Reviews in Mineralogy & Geochemistry
Vol. 76 pp. 135-164, 2013

Thermodynamic Modeling of Fluid-Rock Interaction at Mid-Crustal to Upper-Mantle Conditions

Craig E. Manning

Department of Earth and Space Sciences
University of California, Los Angeles
Los Angeles, California 90095, U.S.A.

manning@ess.ucla.edu

INTRODUCTION

Fluid-rock interaction is important in a wide range of settings in the middle crust to the upper mantle. Fluids are liberated in the crust during prograde metamorphism in convergent-margin settings. At greater depth, devolatilization of subducting lithosphere plays a major role in global element cycling, metasomatic alteration of the mantle, and the genesis of arc magmas. Mafic magmas produced in these settings may stall in the lower crust and liberate volatiles that metasomatize surrounding rocks and trigger production of silicic magmas of crustal derivation. Mounting evidence points to an important role for metasomatic alteration by saline brines in the genesis of some lower-crustal granulite-facies metamorphic terranes.

Unlike shallow geothermal systems or low-grade metamorphic environments, there has been only limited progress in modeling the fluid-rock interaction that characterizes the deeper geologic systems enumerated above. Such phase-equilibrium models require as input the chemical potential, μ_i

$$\mu_i \equiv \left(\frac{\partial G_i}{\partial n_i} \right)_{P,T} \tag{1}$$

of the participating phases or species i, where G_i is the Gibbs free energy of i, n_i is the number of moles of i, P is pressure, and T is temperature. At the P and T of interest,

$$\mu_i = \mu_i^\circ + RT\ln a_i \tag{2}$$

Where μ° is standard state chemical potential, a is activity, R is the gas constant, and T is absolute temperature.

It is challenging to quantify the right-hand terms in Equation (2) at P and T ranging from the middle crust to the upper mantle. This is chiefly because of (1) limitations in our quantitative knowledge of key properties of relevant solutes and H_2O, and (2) uncertainty in how properly to model solute activities at the requisite conditions. As a consequence, aqueous geochemists have been discouraged from plying their trade in the numerous deep geologic systems in which fluid-rock interaction may play a major role in the Earth's chemical and physical evolution.

Here, I discuss strategies for determining the standard-state chemical potential and the activity of a dissolved solute at conditions corresponding to the lower crust and upper mantle. I show that simple approaches can be used to derive reasonable approximations of standard-state properties. The parameters necessary for constraining activity coefficients of aqueous

1529-6466/13/0076-0005$05.00 http://dx.doi.org/10.2138/rmg.2013.76.5

solutes can be calculated or estimated, leading to the conclusion that activity models for dilute aqueous species yield accurate representations of solute behavior at the concentrations observed or predicted in a wide range of H_2O-rich aqueous solutions at high *P* and *T*. This provides the foundation for study of fluid-mineral interaction in a variety of high-*PT* scenarios.

CHEMICAL POTENTIALS OF AQUEOUS SPECIES IN HIGH-*PT* FLUIDS

Standard state chemical potentials of aqueous species

The conventional standard-state for aqueous species in relatively dilute solutions is unit activity of the hypothetical 1.0 molal solution, referenced to infinite dilution. Standard-state thermodynamic properties of an aqueous solute therefore account for the consequences of its transfer to, and influence on, the solvent H_2O. When dissolved in H_2O, an ion such as Na^+ attracts H_2O dipoles so that they form a coordinating cluster, or shell, in which the H_2O molecules are more densely packed and more ordered than they would otherwise be in the ion's absence. For octahedral coordination of H_2O around the sodium ion, we can describe the hydration process as

$$Na^+ + 6H_2O = Na(H_2O)_6^+ \tag{3}$$

Structures such as $Na(H_2O)_6^+$ constitute entities in which the number of H_2O molecules may vary on short time scales but attain some long-term average that varies with *P* and *T*. Accordingly, for the purposes geochemical applications that must address a wide range conditions, it is conventional to neglect the hydration waters when writing reactions (i.e., Na^+, not $Na(H_2O)_6^+$). Any variations in hydration are implicit, and accounted for in the standard state thermodynamic properties of the solutes. This is the same as assuming that the change in any state property associated with Equation (3) is zero.

The Helgeson-Kirkham-Flowers equation of state. The hydration process involves energetic changes that must be taken into account in characterizing the thermodynamic properties of a solute. There are numerous thermodynamic models for the standard state properties of aqueous species (for a review see Dolejš 2013). In geochemistry, the most widely used thermodynamic model is the Helgeson-Kirkham-Flowers equation of state, or HKF EOS (Helgeson and Kirkham 1976; Helgeson et al. 1981; Tanger and Helgeson 1988). The HKF EOS accounts for the energetics of transferring a solute to H_2O as the sum of the intrinsic properties of the solute, the structural change of solvent H_2O around the solute ("collapse", because solution volume decreases), and the electrostatic interactions between the solvent H_2O dipoles and the solute ("solvation"). Hence, the standard Gibbs free energy change of bringing a solute into solution may be written

$$\Delta G_i^\circ = \Delta G_{i,\text{intrinsic}}^\circ + \Delta G_{i,\text{collapse}}^\circ + \Delta G_{i,\text{solvation}}^\circ \tag{4}$$

(All properties considered here are implicitly "conventional"; i.e., relative to those of H^+.) The terms on the right in Equation (4) are not strictly separable (Helgeson and Kirkham 1976). Because solvation effects may be taken into account through electrostatic theory, it is convenient to distinguish them explicitly from nonsolvation effects defined as

$$\Delta G_{\text{non-solvation}}^\circ = \Delta G_{i,\text{intrinsic}}^\circ + \Delta G_{i,\text{collapse}}^\circ \tag{5}$$

This leads to

$$\Delta G_i^\circ = \Delta G_{i,\text{non-solvation}}^\circ + \Delta G_{i,\text{solvation}}^\circ \tag{6}$$

In the HKF EOS, nonsolvation contributions are quantified through species-specific, *P-T* independent EOS coefficients. The solvation contributions are treated via Born theory, which

describes the Gibbs energy change of solvation as a function of the static dielectric constant, $_{H\,O}$, of H_2O:

$$\Delta G^{\circ}_{i,\text{solvation}} = \omega_i \left(\frac{1}{\varepsilon_{H_2O}} - 1 \right) \tag{7}$$

where ω is a species-specific, *P-T* independent EOS coefficient. The requisite parameters have been derived for a wide variety of aqueous species (Shock and Helgeson 1988; Shock et al. 1989; Shock and Helgeson 1990; Shock et al. 1992; Pokrovskii and Helgeson 1995, 1997; Shock et al. 1997; Sverjensky et al. 1997; Plyasunov and Shock 2001). Thus, the Gibbs energies and other thermodynamic properties of solutes can be computed in the HKF EOS framework, provided that the dielectric constant of pure H_2O (Eqn. 7) is well known.

Unfortunately, deploying HKF theory at deep crustal and upper mantle conditions is problematic because ε_{H_2O} has only been measured to 5 kbar and 550 °C (Heger et al. 1980) (Fig. 1). Estimates using the Kirkwood equation (Pitzer 1983; Fernández et al. 1997) or other approaches (Franck et al. 1990) have been employed to extend values of ε_{H_2O} to 10 kbar and 1000 °C, and there has been recent progress in using *ab initio* molecular dynamics to compute ε_{H_2O} to very high pressures (Pan et al. 2013). Nevertheless, the most widely used implementation of the HKF thermodynamic database and computational framework (SUPCRT92, Johnson et al. 1992) is based on the ε_{H_2O} extension of Pitzer (1983), and is limited to a maximum pressure to 5 kbar. The absence of high-*P* ε_{H_2O} data thus prevents use of the HKF EOS to study mineral-fluid equilibria in the high-*PT* environments of interest here.

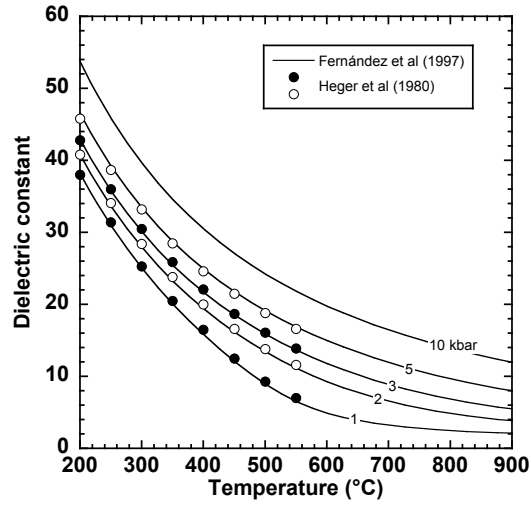

Figure 1. Dielectric constant of H_2O as a function of temperature at constant pressure. Data are from Heger et al. (1980). Solid lines show fitted and extrapolated values from Fernández et al. (1997).

Density models. There are several alternate approaches that can be used to derive high-*P* standard state Gibbs energies of aqueous species (Dolejš 2013). For work at high *P* and *T*, density correlations offer the best prospects because they can be tied to well-calibrated EOS for H_2O (Marshall and Franck 1981; Marshall and Mesmer 1984; Eugster and Baumgartner 1987; Anderson et al. 1991; Dolejš and Manning 2010). Density models are based on the observation that isothermal changes in the logarithms of the equilibrium constants (*K*) for many dissociation reactions display linear correlations with $\log\rho_{H_2O}$. An example is the variation in the equilibrium constant for the self-dissociation of H_2O

$$H_2O = H^+ + OH^- \tag{8}$$

(Sweeton et al. 1974; Marshall and Franck 1981) (Fig. 2). The relations shown in Figure 2 suggest that at constant temperature

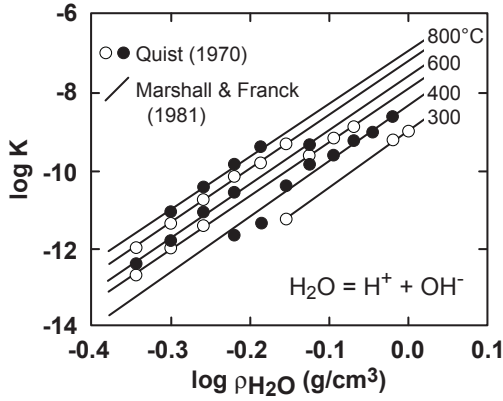

Figure 2. Variation in the equilibrium constant for H_2O self-dissociation with the logarithm of the density of H_2O (g/cm^3). Circles are from Quist (1970). Lines show values calculated using the equation of Marshall and Franck (1981).

$$\log K = m + n \log \rho_{H_2O} \tag{9}$$

where m and n are fit parameters, which may be treated as polynomials in T, e.g.

$$m = m_0 + m_1 T^{-1} + m_2 T^{-2} + m_3 T^{-3} \tag{10}$$

$$n = n_0 + n\, T^{-1} + n_2 T^{-2} \tag{11}$$

(Marshall and Quist 1967; Mesmer et al. 1988; Anderson et al. 1991). Numerous other dissociation reactions display similar behavior, including alkali-halide dissociation (Franck 1956; Quist and Marshall 1968b; Frantz and Marshall 1982; Ho and Palmer 1997), acid and base dissociation (Frantz and Marshall 1984; Mesmer et al. 1988; Mesmer 1991; Ho and Palmer 1997), and the dissolution of oxide and halide minerals (Fournier and Potter 1982; Manning 1994; Caciagli and Manning 2003; Antignano and Manning 2008a,b; Dolejš and Manning 2010).

Manning (1998) showed that log$K$ values for homogeneous and heterogeneous equilibria derived from the HKF EOS also display linear correlations with $\log \rho_{H_2O}$ at high P. Similar behavior was demonstrated for ΔG° for individual aqueous species. Figure 3 gives example correlations, which were derived using SUPCRT92 and thermodynamic data from Pokrovskii and Helgeson (1995). Log$K$ values were computed at 3.0, 3.5, 4.0, 4.5, and 5.0 kbar and 400-600 °C. In Figure 3A, it can be seen that calculated log$K$ for the homogeneous equilibrium $HAlO_2 = H^+ + AlO_2^-$ varies linearly with with $\log \rho_{H_2O}$. Also shown for selected isotherms are the ±0.5 kcal/mol average uncertainties in the predictions estimated by Shock and Helgeson (1988). The distribution of predicted log$K$ values along isotherms is demonstrably linear within the stated uncertainties. Similar results are obtained for the equilibrium constant for corundum hydrolysis and ΔG° of Al^{+3} (Fig. 3), as well as for many other species and equilibria (Manning 1998, 2007; Manning et al. 2010, 2013).

The linear correlations displayed in Figure 3 imply that

$$\left(\frac{\partial \ln K}{\partial \ln \rho_{H_2O}} \right)_T = -\frac{\Delta V^\circ}{RT\beta_{H_2O}} = constant \tag{12}$$

where ΔV° refers to the volume change of the reaction or species of interest and β_{H_2O} is the isothermal compressibility of H_2O. Taking Ca^{+2} as an example, Figure 4 illustrates that the HKF EOS predicts that the ratio in Equation (12) approaches a constant value at pressures ≥ 3 kbar. This is probably because at high P, the nonsolvation contributions to ΔG° approach

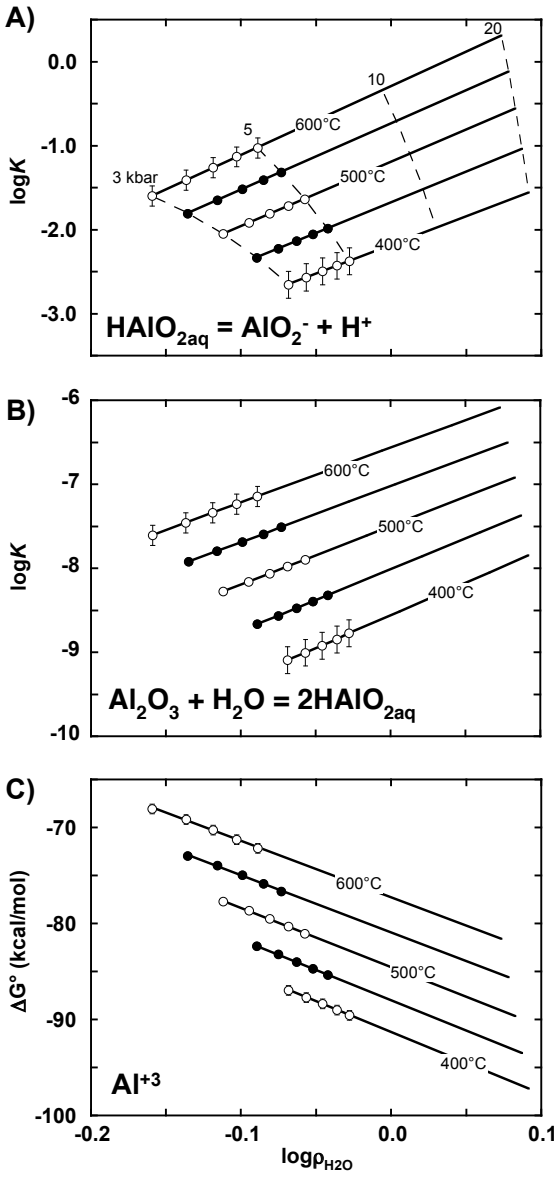

Figure 3. Values of log$K$ and ΔG° vs. $\log \rho_{H_2O}$ (in g/cm^3) illustrating density-based extrapolations for a representative homogeneous equilibrium (A), heterogeneous equilibrium (B), and single species (C). Data from Pokrovskii and Helgeson (1995) were employed with SUPCRT92 to compute properties at 3-5 kbar (500 bar increments) at 400-600 °C (50 °C increments). Solid lines represent linear fits to calculated properties along each isotherm, extrapolated to 20 kbar. Dashed lines in (A) show isobars. Representative error bars correspond to ±0.5 kcal/mol (Shock and Helgeson 1988).

constant values while the solvation contributions depend on ε_{H_2O} which is strongly correlated with ρ_{H_2O} (Dolejš and Manning 2010).

The nearly linear isothermal variation of log$K$ and ΔG° with $\log \rho_{H_2O}$ to 5 kbar supports extrapolation to higher P (Fig. 3). It is not expected that behavior is exactly linear, but several arguments support the conclusion that such extrapolations are reasonable approximations of high-PT thermodynamic properties. First, the range of ρ_{H_2O} over which the extrapolation is performed is relatively small, owing to the progressively decreasing compressibility of H_2O. At any T, the difference in $\log \rho_{H_2O}$ between 3 and 5 kbar is about the same as that between 5 and 10 kbar and about half that between 5 and 20 kbar (Fig. 3A). Second, variations in the density of water are significantly less nonlinear at the high pressures of interest than in the vicinity of the critical point. Neither discontinuities nor strong variations in derivative properties occur in dense H_2O. Finally, the uncertainties in log$K$ and ΔG° are large relative to potential nonlinearity. Higher order fits are not justified at the accuracy level of the predictions.

Activity models for aqueous species

Activity models have also been a major limitation to high-PT studies of aqueous chemistry, fluid-rock interaction, and reactive fluid flow. The activity of a solute accounts for the energetic consequence of departure from standard-state behavior due to interactions with other solutes present at finite concentration. Activity is related to concentration through

$$a_i = \gamma_i m_i \qquad (13)$$

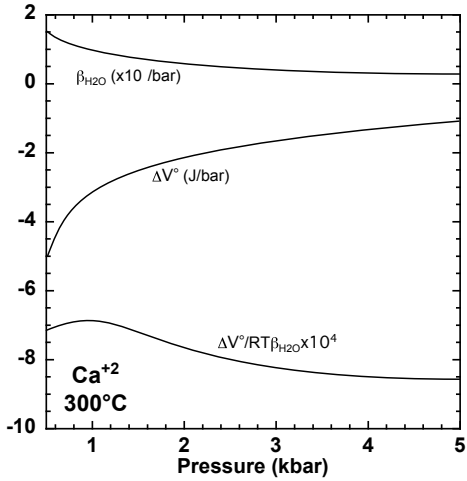

Figure 4. Isothermal variation at 300 °C of the compressibility of H_2O, the standard molal volume of Ca^{+2}, and their ratio multiplied by $1/RT$. The ratio approaches a constant value at $P > 3$ kbar, consistent with the linear slopes in Figure 3 (see text). Data from Helgeson and Kirkham (1974) and SUPCRT92.

where γ_i is the activity coefficient and m_i is molal concentration. (Alternate concentration scales are necessary at very high solute concentrations.)

In addition to the interactions with H_2O discussed above, solutes will also interact with each other, and the magnitudes of these interactions may vary significantly depending on solute identities. The largest energetic contributions arise from coulombic forces operating on solute ions. The hydrated ions of a simple electrolyte like NaCl exert forces of attraction and repulsion on each other over relatively large distance, leading to nonrandom ion distributions in the solution. The resulting average cluster distribution has lower energy than would a random distribution in an ideal solution. The chemical potential of each ionic solute at finite but low concentration is thus lower than in it would be if $\gamma_i = 1$, requiring that the activity coefficient is less than unity. The number of hydrated clusters increases with rising electrolyte concentration. Because the magnitudes of coulombic forces vary with the inverse of separation distance, progressively tighter packing of the charged clusters leads to progressively greater negative departures from ideality, and hence decreasing activity coefficients.

With continued increase in the concentration of a dissociated NaCl electrolyte in H_2O, the ion abundance eventually becomes so great that two effects cause activity to cease decreasing, and then to rise. First, the added ions eventually involve so much H_2O in the formation of hydration shells that availability for further hydration is affected. In addition, in tightly packed ionic solutions the domination of repulsive over attractive forces reduces "ordering", which diminishes the departure from ideality. Note that in this hypothetical process, the effects of association of ions are ignored; i.e., we are taking no account of the possibility of $Na^+ + Cl^- = NaCl_{(aq)}$, the forward progress of which will limit the rise in ion concentration.

Estimation of activity coefficients for geochemical applications has chiefly followed two separate lines of investigation. One approach has been the development of "specific-ion interaction" approaches based on virial equations (e.g., Pitzer 1977, 1979). This method is largely empirical and does not account for the different species of a particular solute ion that may be present in solution; i.e., the concentration of Na^+ or Cl^- is equivalent to the total concentration of Na or Cl. Virial equations are especially useful at very high concentrations, for example in evaporite brines, but they preclude evaluation of the contributions of distinct solute forms of the same element to the interactions among solutions and minerals. Moreover, the empirical nature of virial approaches means that a substantial body of experimental data is required to implement the approach. Such a body of data simply does not exist at high P and T.

Ion activity models are generally based on a version of the Debye-Hückel equation, which was developed for a solution of completely dissociated ions. These models take the form

$$\log \gamma_i = -\frac{A z_i^2 \sqrt{I}}{1 + \text{å}_i B \sqrt{I}} + b_i I \tag{14}$$

where A and B are solvent parameters, z_i is the ion charge, å_i is the ion size parameter (in cm), b_i is a constant characteristic of the electrolyte and dependent on P and T, and I is ionic strength.

Ionic strength is computed from

$$I = \frac{1}{2} \sum_i m_i z_i^2 \tag{15}$$

and has units of concentration, here molality. Debye-Hückel-type equations were developed for solutions without ion pairing. However, significant ion pairing is expected at high P and T (see below). This can be accounted for by including only unpaired ions in the summation (e.g., Helgeson 1969; Helgeson et al. 1981). In this case, I is termed the "true" ionic strength.

In Equation (14), the å parameter is nominally a function of electrostatic radius and hence could vary with P and T. However, Helgeson et al. (1981) showed that this need not be considered. The A and B solvent parameters are defined by

$$A \equiv \frac{\left(2\pi N \rho_{H_2O}\right)^{\frac{1}{2}} e^3}{2.303 \times 1000^{\frac{1}{2}} \left(\varepsilon_{H_2O} kT\right)^{\frac{3}{2}}} = \frac{1.825 \times 10^6 \left(\rho_{H_2O}\right)^{\frac{1}{2}}}{\left(\varepsilon_{H_2O} T\right)^{\frac{3}{2}}} \tag{16}$$

and

$$B \equiv \left(\frac{8\pi N \rho_{H_2O} e^2}{1000 \varepsilon_{H_2O} kT}\right)^{\frac{1}{2}} = \frac{5.029 \times 10^9 \left(\rho_{H_2O}\right)^{\frac{1}{2}}}{\left(\varepsilon_{H_2O} T\right)^{\frac{1}{2}}} \tag{17}$$

(e.g., Helgeson and Kirkham 1974), where N is Avagadro's number, e is electron charge, k is Boltzmann's constant, and T is absolute temperature. Dimensions of A and B are $kg^{1/2}\ mol^{-1/2}$ and $kg^{1/2}\ mol^{-1/2}\ cm^{-1}$, respectively.

Equations (16) and (17) demonstrate that A and B depend on H_2O density and dielectric constant. As discussed above, while ρ_{H_2O} is reasonably well known from H_2O equations of state (e.g., Haar et al. 1984; Saul and Wagner 1989; Wagner and Pruß 2002), ε_{H_2O} is not. However, estimates of A and B may be made from extrapolations of ε_{H_2O} to high P and T (Fig. 1). Figure 5 shows values of A and B from Manning et al. (2013).

Attempts to use Equation (14) have a long and storied history in solution chemistry in general, and aqueous geochemistry in particular. The various, widely used forms of Equation (14) can be derived from simplifying assumptions. For example, the Debye-Hückel equation is obtained if $b_i = 0$. Assuming $\text{å}_i B = 1$ and $b_i = 0$ yields the Güntelberg equation. Because positive values of b_i are required for γ_i to increase in concentrated solutions, the Debye-Hückel and Güntelberg equations nominally pertain to electrolyte behavior only in dilute solutions. This problem is partly circumvented by the Davies (1938, 1962) equation, in which $\text{å}_i B = 1$ and $b_i = CAz^2$ where C is 0.2 or 0.3. But the appropriateness of using these (or any other) fixed values of C might logically be questioned at high P and T.

Recognizing the importance of investigating fluid-rock interaction in geological settings of widely varying P and T, Helgeson and coworkers (Helgeson 1969; Helgeson et al. 1981) de-

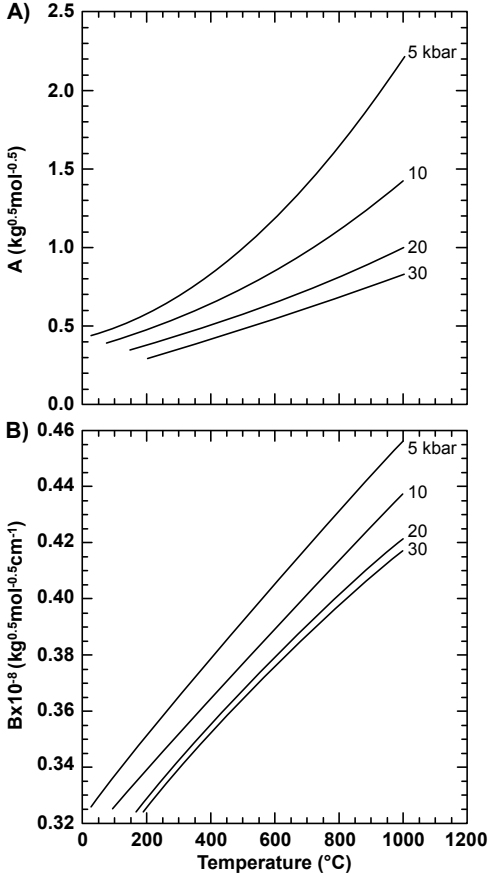

Figure 5. Variation in the *A* and *B* solute parameters with temperature at a range of pressures (from Manning et al. 2013).

veloped a framework in which values of the b_i parameter (variably referred to as the "extended term parameter," or "B-dot" after an alternate symbol definition) were derived for a wide range of electrolytes as a function of *P* and *T*. In practice, it is impractical to account separately for å and *b* for each ion, so it is typically assumed that these parameters may be approximated as those of the dominant electrolyte in solution, which for geochemical applications is in many cases NaCl. As with the *A* and *B* parameters, b_{NaCl} has been limited to ≤5 kbar (Helgeson et al. 1981). However, Manning et al. (2013) recently used correlations with ρ_{H_2O} to extrapolate b_{NaCl} to high *P* and *T* (Fig. 6).

Activity coefficients calculated from the various modifications of Equation (14) differ dramatically. Figure 7 shows calculated activity coefficient for a monovalent ion (e.g., Na^+ or Cl^-) at 700 °C, 10 kbar, conditions relevant to the high-*PT* environments under consideration here. At these conditions, A = 1.0 $kg^{1/2}/mol^{1/2}$, B = 0.4×10^{-8} $kg^{1/2}/mol^{1/2}cm$, å = 3.72×10^{-8} cm, and b_{NaCl} = 0.28 kg/mol (Figs. 5 and 6; Manning et al. 2013). The Güntelberg equation is similar to the Debye-Hückel equation and yields steadily decreasing value of γ_i with rising ionic strength. In contrast, the Davies and B-dot equations yield similar forms, with minima at I = 0.5-0.8 molal and rapid rise in activity coefficient at higher *I*.

COMPARISON OF EXPERIMENTAL AND CALCULATED MINERAL SOLUBILITY

Taken together, the need for extrapolations of log*K* and $\Delta G°$, the disparate forms of solute activity models, and the uncertainties in solute parameters might discourage any attempt to carry out quantitative modeling of speciation, mineral solubility, and/or reactive transport in high-*P* environments. Such reservations would be strengthened by absence of experimental data with which to test the accuracy of any models. However, with the developments of hydrothermal-piston cylinder methods (Ayers et al. 1992; Manning 1994; Manning and Boettcher 1994) and hydrothermal diamond-anvil cell techniques (Bassett et al. 1996), there is now a growing data set on high-*PT* mineral solubility that can be used to assess the computational approaches

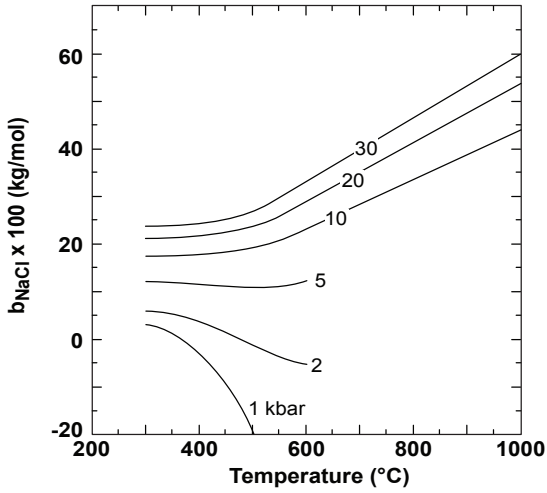

Figure 6. Variation in the extended term parameter for NaCl with temperature at a range of pressures (from Manning et al. 2013).

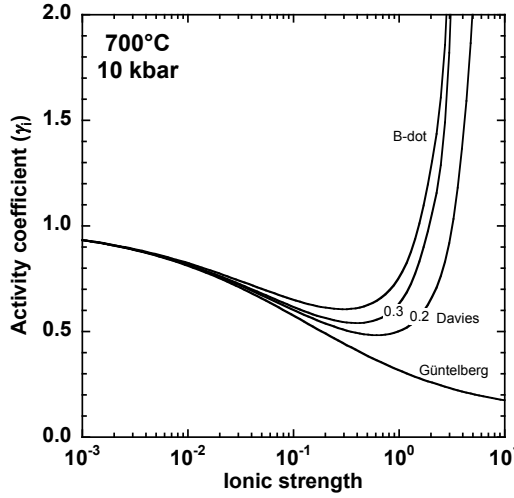

Figure 7. Comparison of activity models for monovalent ions at 700 °C, 10 kbar. Parameter values: A = 1.0 $kg^{1/2}/mol^{1/2}$, $B = 0.4\times10^{-8}$ $kg^{1/2}/mol^{1/2}cm$, å = 3.72×10^{-8} cm, and b_{NaCl} = 0.28 kg/mol (Figs. 5 and 6; Manning et al. 2013).

outlined above at mid-crustal to upper-mantle conditions. A simple example serves to show that in nearly every respect, concerns about extending these methods to the lower crust and upper mantle are largely misplaced.

The solubility of corundum in H_2O and in KOH solutions has been measured at 700 °C, 10 kbar, to a total K concentration ($[K]_{total}$) of ~4 molal (Becker et al. 1983; Tropper and Manning 2007a; Wohlers and Manning 2009). The data allow evaluation of the density extrapolation method and of the consequences of adopting different activity-coefficient models. For these solutions we can assume the presence of seven main aqueous species in solution: H^+, OH^-, K^+, $KOH_{(aq)}$, $HAlO_{2(aq)}$, AlO_2^-, and $KAlO_{2(aq)}$. The density model can be used to derive equilibrium constants from SUPCRT92 and Ho and Palmer (1997) at 700 °C, 10 kbar, for the following equilibria:

$$\underset{corundum}{Al_2O_3} + 2H_2O = 2HAlO_2 \qquad \log K = -5.883 \tag{18}$$

$$HAlO_{2(aq)} = H^+ + AlO_2^- \qquad \log K = -4.877 \tag{19}$$

$$KOH_{(aq)} = K^+ + OH^- \qquad \log K = -1.206 \tag{20}$$

$$KAlO_{2(aq)} = K^+ + AlO_2^- \qquad \log K = -0.299 \tag{21}$$

(Wohlers and Manning 2009). Using these equilibrium constants, the log$K$ for Equation (8) (Marshall and Franck 1981), the constraint of electrical neutrality, one of the ion-activity models, and known $[K]_{total}$, the solubility of corundum in H_2O and aqueous KOH solutions can be computed independent of the experiments by iterative solution of the resulting system of equations.

Becker et al. (1983) and Tropper and Manning (2007a) reported corundum solubility in pure H_2O at 700 °C, 10 kbar, to be 1.08±0.08 and 1.19±0.14 millimolal, respectively. Using the Güntelberg equation for ion activity coefficients, A = 1.0, and unit activity coefficients for neutral species, the predicted solubility derived from the density extrapolation is 1.14 millimolal, in close agreement with the measured values. Other activity formulations give an essentially identical result because the solution is so dilute (Fig. 7).

While the result above is encouraging, the low total solubility of corundum in pure H_2O means that the comparison does not meaningfully distinguish potential differences between activity models. For this it is necessary to compare predicted and calculated solubility as a function of increasing concentration of an electrolyte such as KOH. Figure 8 shows corundum solubilities measured in KOH solutions at 700 °C, 10 kbar (Wohlers and Manning 2009) and those independently calculated using the Güntelberg, Davies (C = 0.2 and 0.3) and B-dot formulations for activity coefficient. Parameter values were the same as those used in Figure 7, and it was again assumed that $\gamma = 1$ for neutral species. The various equations for ion activity coefficient yield calculated solubilities that differ negligibly from one another at $[K]_{total} \leq 0.1$ molal (Fig. 8). But even at the highest $[K]_{total}$ of 4 molal, predicted $[Al]_{total}$ ranges from a minimum of 2.0 molal (Davies with $C = 0.3$) to 2.4 molal (Güntelberg) as compared to the experimental value of 2.7 molal, a surprisingly small difference given the high concentration. In general, it is clear that differences in predicted solubility arising from adopting any of the activity models are minor over a wide range of concentration and ionic strength. Note that Wohlers and Manning (2009) used the Güntelberg formulation to refine the log$K$ for Equation (21), which explains why corundum solubility calculated using Güntelberg activity coefficients best matches the experimental data (Fig. 8); however, the relative differences between the formulations would remain similar if one of the other activity models had been used.

Both the Güntelberg and Davies formulations depend on knowledge of only one solvent parameter, A. Manning and coworkers have argued that calculations of mineral solubility at high P and T are relatively insensitive to variations in A, and that it can be assumed equal to unity (Manning 1998, 2007; Wohlers and Manning 2009; Manning et al. 2010; Wohlers et al. 2011). This is supported by the relatively narrow range in values exhibited by A away from the critical region of H_2O (Fig. 5A) (Helgeson and Kirkham 1974), and by tests indicating that results varied little with changes in this parameter. But assuming A = 1.0 may have been fortuitous, as Figure 5A shows that the new high-P estimations yield A = 1.0 at 700 °C, 10 kbar. As a check, values of A were arbitrarily varied by ±20%, and corundum solubility was then recalculated and compared to the experiments of Wohlers and Manning (2009). Figure 9 illustrates that the calculations are insensitive to relatively extreme and arbitrary variations in A. Although accurate knowledge of this parameter is useful for high precision, uncertainties in A should not prevent thermodynamic modeling of aqueous solutions at high P and T.

The insensitivity of calculated solubility to activity-model form or solvent parameters is due at least in part to the effects of ion pairing. As will be shown below, ion pair formation in H_2O is significantly more extensive at high P and T than in surficial or shallow crustal settings. This will tend to limit the rise in true ionic strength, at least in compositionally simple systems.

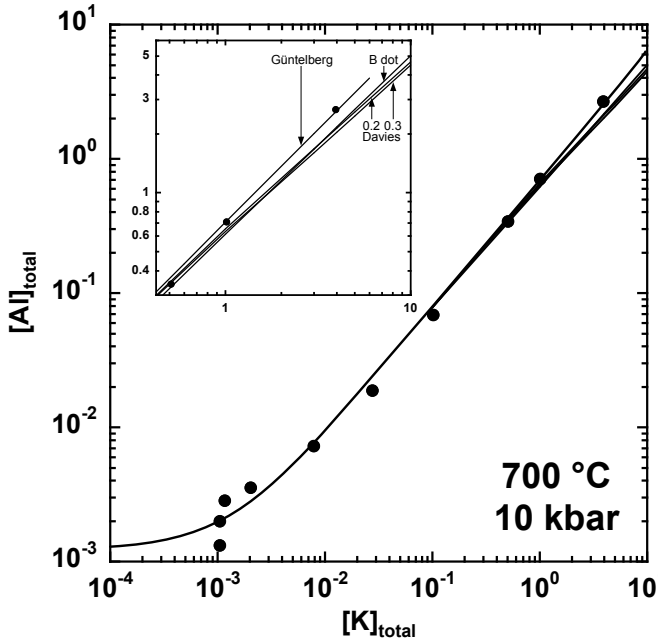

Figure 8. Comparison of experimentally determined corundum solubility in KOH solutions with independently calculated solubility using different ion activity models, at 700 °C, 10 kbar. Filled circles are data of Wohlers and Manning (2009); solid lines are calculated solubility according to the Güntelberg, Davies, and B-dot equations (see text). Inset shows expanded view of high-concentration range. Parameter values: A = 1.0 kg$^{1/2}$/mol$^{1/2}$, B = 0.4×10^{-8} kg$^{1/2}$/mol$^{1/2}$cm, å = 3.72×10^{-8} cm, and b = 0.28 kg/mol (Figs. 5 and 6; Manning et al. 2013).

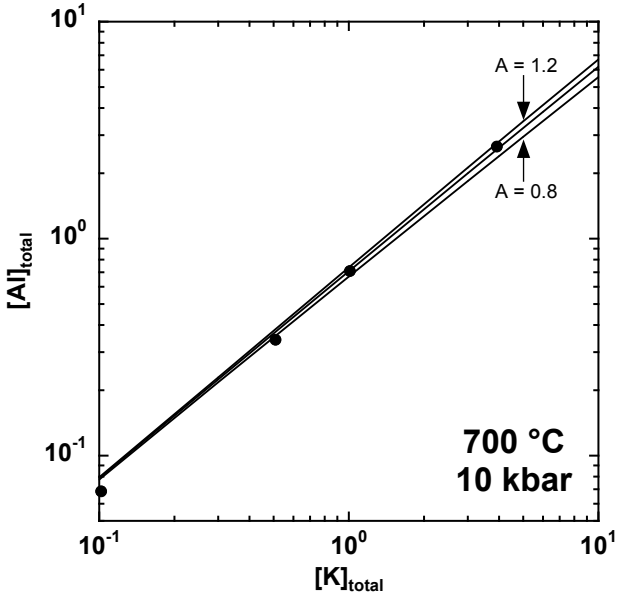

Figure 9. Effect of varying A parameter on calculated corundum solubility at 700 °C, 10 kbar. Activities calculated using the Güntelberg equation. Experimental data from Wohlers and Manning (2009).

The example of corundum solubility in H_2O and KOH solutions suggests that use of density-based models to extrapolate standard state thermodynamic data, when coupled with the observation that speciation calculations are relatively insensitive to choice of activity model and solute parameters, is a promising approach for calculation of mineral solubility at high P and T. Similar results have been obtained for calcite in H_2O at a range of high P and T (Manning et al. 2013) and albite + paragonite + quartz in H_2O at 10 kbar and $T < 500$ °C (Manning et al. 2010) (see below).

Several important caveats should be noted. The calculations outlined above incorporate data from a variety of sources; no attempt at internal consistency was made. Use of the density-based fitting procedure for extrapolation to high P can lead to subtle but potentially aggravating inconsistencies with calculations at 3-5 kbar using unsmoothed thermodynamic data (e.g., from SUPCRT92). More fundamentally, the derivation of the properties of aqueous species or equilibria from solubility or conductance data may lead to nonunique solutions that depend on a priori assumptions about the identities of participating species. An example is NaCl, for which the same data sets have been used to obtain fundamentally different conclusions about its extent of dissociation at low to moderate P (c.f. Frantz and Marshall 1984; Oelkers and Helgeson 1991). Results of calculations of species abundances are frequently provisional, subject to significant refinement upon the arrival of more and better experimental data. Nevertheless, it is clear from the tests above that reasonably accurate estimates of equilibrium constants and activity coefficients can be made and applied to investigate metasomatic environments ranging from the middle crust to the upper mantle.

APPLICATIONS

The agreements between experimentally determined mineral solubility at high P and T on one hand, with those predicted using the density model and a combination of the HKF EOS and low-P experimental data on the other, lends confidence to the quantitative investigation of fluid-rock interaction at $P > 5$ kbar. Below I discuss examples that highlight the utility of extending many of the tools familiar to those working at lower P to the high-P environments of interest here.

Activity-activity diagrams

Standard state properties of ions, H_2O, and minerals can be used to compute equilibrium activity-activity diagrams, which are useful for illustrating metasomatic phase relations at a P and T of interest (e.g., Bowers et al. 1984). Such diagrams are projections of mineral saturation surfaces onto a coordinate system involving fluid compositional variables. For example, consider the equilbrium

$$\underset{\textit{K-feldspar}}{3KAlSi_3O_8} + 2H^+ = \underset{\textit{muscovite}}{KAl_3Si_3O_{10}(OH)_2} + 2K^+ + 6SiO_{2(aq)} \quad (22)$$

Here, the equilibrium is written so that Al is conserved in the minerals, and $SiO_{2(aq)}$ corresponds to total SiO_2 in solution, neglecting polymeric silica speciation (see below). The logarithm of the equilibrium constant for Equation (22) is

$$\log K = 2\log\frac{a_{K^+}}{a_{H^+}} + 6\log a_{SiO_{2(aq)}} + \log a_{\text{muscovite}} - \log a_{\text{K-feldspar}} \quad (23)$$

Assuming pure, stoichiometric minerals in their standard state of unit activity at any P and T, the two right-hand terms equal zero, and Equation (23) can be rearranged to obtain

$$\log\frac{a_{K^+}}{a_{H^+}} = \frac{1}{2}\log K - 3\log a_{SiO_{2(aq)}} \quad (24)$$

which is the equation for a straight line if we adopt plotting coordinates of $\log(a_{K+}/a_{H+})$ and $\log a_{SiO_{2(aq)}}$. Writing similar Al-conserving reactions between minerals in the system of interest (e.g., K_2O-Al_2O_3-SiO_2-H_2O, or KASH) and then computing equilibrium constants from standard state thermodynamic properties allows identification of equilibrium mineral stability fields and phase boundaries as functions of fluid compositional variables.

Figure 10A illustrates equilibrium fluid-mineral phase relations in the KASH system at 700 °C, 10 kbar. At constant *P* and *T*, the saturation surface for each stable aluminum-bearing mineral defines a divariant field; mineral-mineral phase boundaries yield univariant phase boundaries; assemblages of three minerals are invariant. Quartz is Al-free (neglecting trace substitution), so it defines a saturation surface which projects onto Figure 10A as a vertical line. Because the diagram portrays equilibrium phase relations, quartz saturation defines the upper limit of $SiO_{2(aq)}$ activity, and any fluid with higher a_{SiO_2} is metastably supersaturated with respect to quartz. The diagram is useful for exploring how isothermal-isobaric changes in mineral assemblages record variation in activities of aqueous species at local equilibrium, which aids interpretation of metasomatic mineral zoning observed in outcrop. For example, at constant *P* and *T*, mineral zonation from quartz + kyanite → kyanite + muscovite →

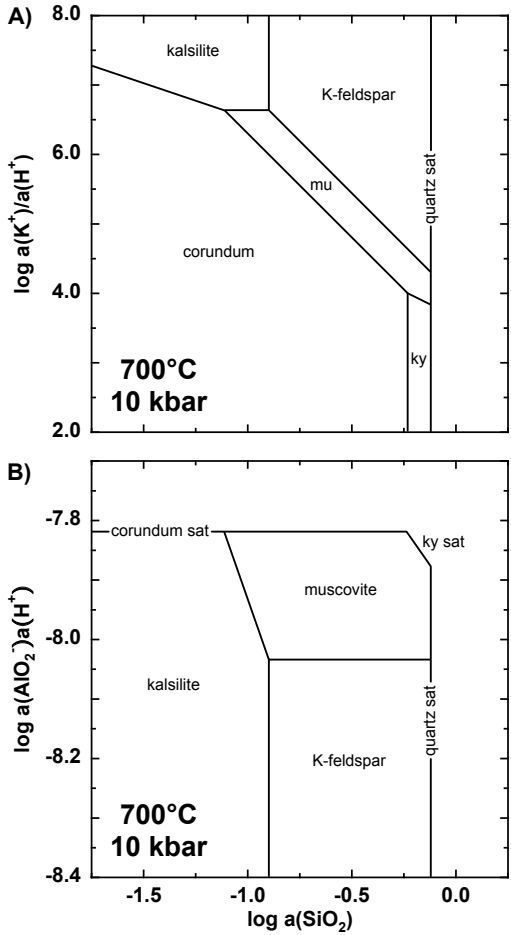

Figure 10. Equilibrium activity-activity diagrams depicting phase relations among minerals and H_2O in the system K_2O-Al_2O_3-SiO_2-H_2O at 700 °C, 10 kbar. Sources of thermodynamic data: minerals, Holland and Powell (1998; 2002 update, as implemented in the PERPLEX software package (*http://www.perplex.ethz.ch*)); H_2O, Haar et al. (1984); Al and K species, density-based extrapolations of data from Pokrovskii and Helgeson (1997); SiO_2, Manning (1994). Abbreviations: mu, muscovite; ky, kyanite; sat, saturation.

muscovite + corundum indicates decreasing a_{SiO_2} and rising a_{K+}/a_{H+} in the coexisting pore fluid. At quartz saturation, rising acidity along a flow path at constant a_{K+} would produce mineral zoning of K-feldspar → muscovite → kyanite.

The choice of species is arbitrary and strictly a matter of convenience. Common practice is use of the simple cations of the oxides of interest, except for silica. However, these need not—and in many cases at high *P* and *T*, do not—correspond to the most abundant species in solution. Species choice is immaterial because the topology of the fluid-mineral phase relations must be the same, though the numeric values of the activity ratios and products change. Figure 10B illustrates phase relations in the KASH system, again at 700 °C and 10 kbar, but with the aqueous Al species AlO_2^-. As described above, this species is likely to predominate in high-*PT* fluids in this system at pH only slightly above neutrality. Nevertheless, the topology is the same as if Al^{+3} were used instead. Examples of other quantitative high-*PT* activity-activity diagrams can be found in Manning (1998, 2007).

Homogeneous equilibria

Experimental data constraining the equilibrium constant for the self-dissociation of water (Eqn. 8) (Quist 1970; Sweeton et al. 1974) have been fit using a density model (Marshall and Franck 1981). Figure 11 shows variation in the equilibrium constant (log*K*) for Reaction (8) with pressure along isotherms (200, 400, 600, 800 °C), and along geothermal gradients (10, 20, 40 °C/km) that model *dP/dT* associated with burial/exhumation and heating/cooling in a range of crustal and upper-mantle settings. It can be seen that log*K* becomes less negative with increasing *P* along the plotted isotherms, with increasing *T* along isobars, and with greater burial along geotherms. This means that Reaction (8) is driven to the right to ever-greater degrees with progress along these paths; that is, the self-dissociation of water becomes more extensive. The opposite obtains for cooling and decompression paths.

The greater extent of H_2O self-dissociation in high *P-T* environments has important consequences. Figure 11 shows that neutral pH is dramatically lower than in shallower environments. In addition, in contrast to shallow-crustal environments, the H_2O self-dissociation products H^+ and OH^- contribute significantly to ionic strength in deep crustal environments. For example, at 600 °C and 25 kbar, conditions that may be expected to attain along the tops of subducting slabs (e.g., Syracuse et al. 2010), the ionic strength of pure H_2O is ~1 millimolal.

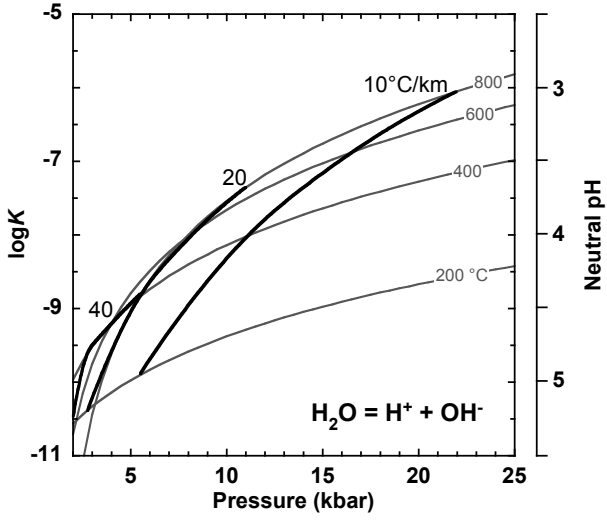

Figure 11. Variation in the equilibrium constant for H_2O self-dissociation with pressure along isotherms (light gray lines) and model linear geotherms (bold lines). Values of log*K* calculated from Marshall and Franck (1981). Neutral pH is displayed on the right, assuming unit activity coefficients of H^+ and OH^-.

NaCl is likely to be an important electrolyte in high *P-T* environments. Figure 12A illustrates that the equilibrium constant for

$$NaCl_{(aq)} = Na^{+} + Cl^{-} \tag{25}$$

rises with increasing depth along any isotherm (Quist and Marshall 1968a). In contrast, the coupled rise in *P* and *T* with burial along a geotherm leads to a decrease in log*K*.

The extent of dissociation of electrolyte *AB* is usefully characterized as

$$\alpha_{AB} \equiv 1 - \frac{\left[AB_{(aq)}\right]}{\left[AB\right]_{total}} \tag{26}$$

Where $[AB_{(aq)}]$ and $[AB]_{total}$ denote the concentration of associated electrolyte in the solution, and the electrolyte total concentration, respectively. According to Equation (26), α_{AB} varies from 0 to 1 as electrolyte *AB* changes from fully associated to fully dissociated, and it therefore represents a simple parameter for tracking the extent of electrolyte dissociation or association.

Figure 12B illustrates the variation in α_{NaCl} with *P* along the same isotherms and geotherms as in Figure 12A, assuming dilute solutions in which activity coefficients can be approximated

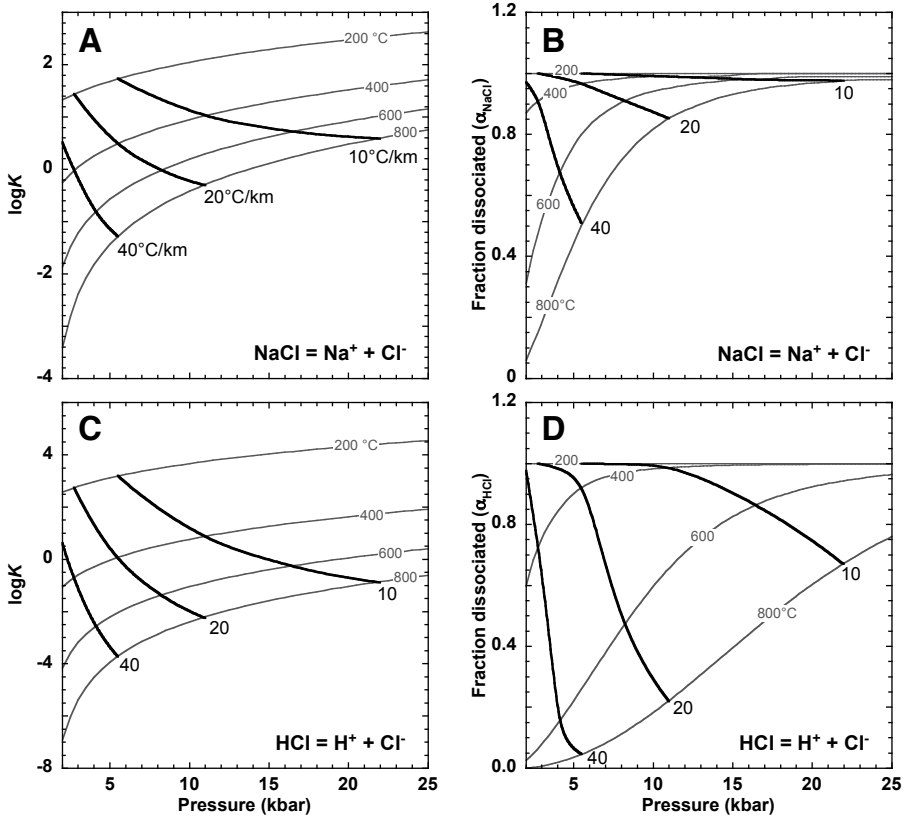

Figure 12. Variation in equilibrium constant and dissociation parameter (a) for NaCl (A and B) and HCl (C and D) along isotherms (light gray lines) and model geotherms (bold black lines) (Quist and Marshall 1968a; Frantz and Marshall 1984). Activity coefficients assumed to be 1.

as unity. The extent of dissociation rises with P along isotherms. With isobaric heating at <5 kbar, NaCl changes from fully dissociated at low T to strongly associated at high T. This contrasts with behavior along the same path at high P, where less association is induced by heating. These relations mean that solute NaCl compressed along model geothermal gradients is more dissociated than it would be if isobarically heated to the same extent. In general, the extent of NaCl association is greater at all elevated P and T than at 25 °C and 1 bar, but when high-T igneous and metamorphic environments are compared, the extent of electrolyte dissociation is greater in deep settings (e.g., subduction zones) than in their shallow equivalents (e.g., contact metamorphic aureoles).

At fixed P and T, rising NaCl concentration in dilute solutions will initially inhibit dissociation, owing to the decrease in activity coefficient (Fig. 7). However, continued increase in concentration will eventually cause activity coefficients to exceed unity and yield more extensive dissociation. In the saline brines that may accompany metamorphism and melting in deep-crustal amphibolites and granulites (Touret 1985; Newton et al. 1998; Aranovich et al. 2013), NaCl is effectively completely dissociated (Aranovich and Newton 1996) (see below). Similar observations can be made for KCl (Aranovich and Newton 1997; Ho and Palmer 1997), as well as for AB_2 electrolytes such as $CaCl_2$ and $MgCl_2$ (Fig. 13) (Frantz and Marshall 1982).

At ambient conditions HCl is a strong acid by virtue of its large log$K$ of 9.3, which indicates nearly complete dissociation. However, Frantz and Marshall (1984) showed that HCl becomes much weaker at high P and T. Figure 12C illustrates that variation in log$K$ along isotherms and geotherms is similar to that of NaCl, although values exhibit a wider range. The equilibrium constants translate to α_{HCl} indicating that burial along all geotherms yields significant HCl association (Fig. 12D). The extent of association is greatest along elevated geotherms, but is still prounounced even along subduction-type geotherms that are here modeled as 10 °C/km. Similar effects can be seen in strong bases such as KOH (Ho and Palmer 1997). In general, strong acids and bases become significantly weaker in high P-T fluids.

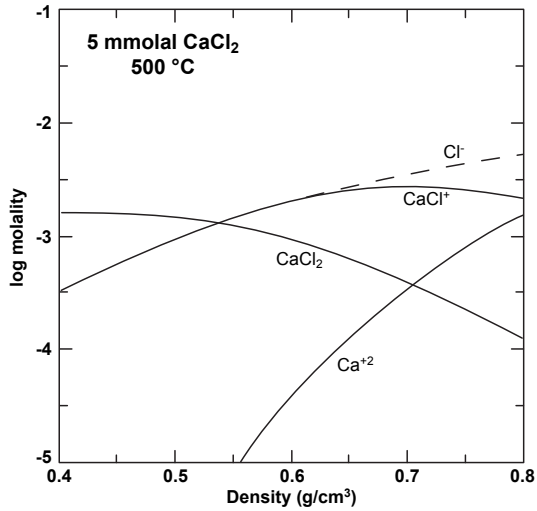

Figure 13. Species abundances in a 0.005 molal $CaCl_2$ solution at 500 °C, as a function of H_2O density (Frantz and Marshall 1982).

The pH dependence of mineral solubility

Mineral dissolution in H_2O is a strong function of pH. However, the substantial changes with P and T in H_2O self-dissociation and in mineral and solute stabilities translate to differences in the pH dependence of mineral dissolution. This can be seen using two examples, calcite and corundum.

Calcite dissolution is the primary contributor to groundwater alkalinity, but the magnitude of this effect depends on the prevailing pH and the relative stabilities of $CO_{2(aq)}$, HCO_3^- and

CO_3^{-2}. This effect arises from the modest solubility of calcite in H_2O, which can be seen by writing the equilibria

$$\underset{calcite}{CaCO_3} = Ca^{+2} + CO_3^{-2} \quad (27)$$

$$HCO_3^- = H^+ + CO_3^{-2} \quad (28)$$

$$CO_{2(aq)} + H_2O = H^+ + HCO_3^- \quad (29)$$

Equilibrium constants for Equations (27-29) can be combined with Equation (8) and charge and mass balance to derive the well-known pH dependence of calcite solubility (Fig. 14A). Calcite solubility corresponds to the sum of all carbonate species in solution, which together must equal the total dissolved calcium (only Ca^{+2} is considered for simplicity). The minimum calcite solubility of 0.06 millimolal exists in alkaline solutions of pH >12. However, decreasing pH progressively increases solubility as Equations (28) and (29) are driven to the left due to H^+ addition. Figure 14A illustrates that reaction with acidic solutions can yield very high

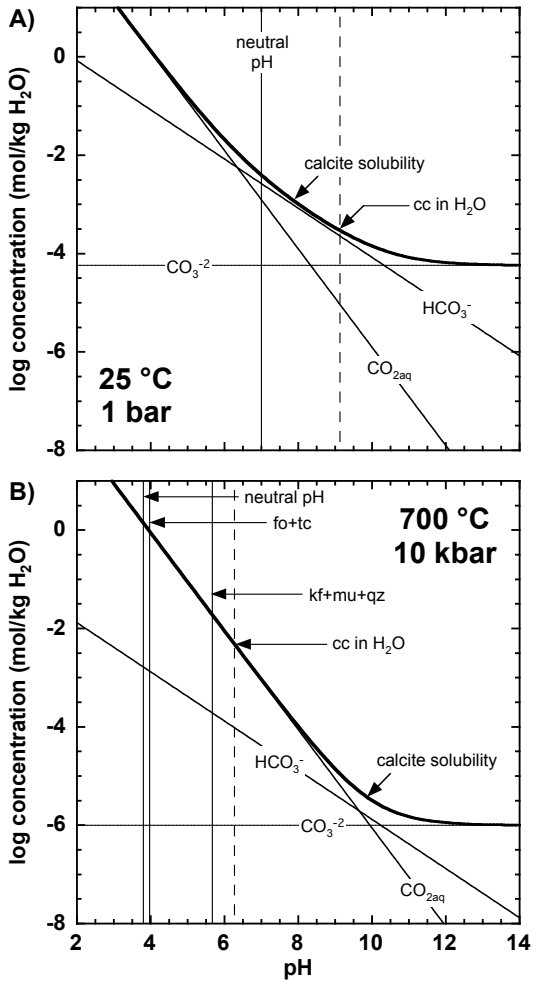

Figure 14. Solubility of calcite as a function of pH at 25 °C, 1 bar (A), and 700 °C, 10 kbar (B). Calcite solubility (bold line) is the sum of the concentrations of the carbonate species (thin lines). Vertical dashed lines show pH in pure H_2O equilibrated with calcite; intersections with bold curves define the solubility of calcite in H_2O. Vertical solid lines are neutral pH and pH values imposed by relevant silicate mineral buffers (see text). Figures calculated assuming unit activity coefficients and the only calcium species is Ca^{+2}. Calculations in (B) used density extrapolation methods with data from Marshall and Frank (1981) and SUPCRT92 using the slop98 data set. Abbreviations: cc, calcite; fo, forsterite; kf, K-feldspar; mu, muscovite; qz, quartz; tc, talc.

calcite solubility. In the absence of external controls on pH, initially neutral H_2O brought into equilibrium with calcite acquires a pH of 9.1 at ambient conditions, solubility is 0.30 millimolal, and the predominant form of dissolved carbon will be HCO_3^-.

Calcite solubility relations exhibit similar form at deep-crustal conditions of 700 °C and 10 kbar (Fig. 14B). Solubility is at a minimum in alkaline solutions, and it increases with decreasing pH. In addition, calcite solubility is essentially identical in the most acidic solutions at the two *P-T* conditions shown. However, there are three important differences from relations at ambient conditions. First, the minimum solubility in alkaline solutions is predicted to be *lower* than at 25 °C, 1 bar. Second, the relative stabilities of the carbonate species vary with *P* and *T*, and it can be seen that the HCO_3^- predominates over a narrower pH range at 700 °C than at ambient conditions. Finally, the pH of initially pure H_2O equilibrated with calcite shifts to 6.2 relative to neutral pH of 3.8 at these conditions. The magnitude of the shift is similar to that at 25 °C, 1 bar, but the solubility of 11 millimolal at the acquired pH is higher and the predominant dissolved carbon species is carbonic acid ($CO_{2(aq)}$).

In contrast to carbonate minerals, aluminum-oxide compounds are amphoteric owing to the ability of dissolved Al and its hydrates to form stable cations and anions. The effects of changing *P* and *T* from ambient conditions to those of the deep crust and upper mantle can be examined using corundum (Al_2O_3). In the presence of H_2O, corundum is metastable with respect to gibbsite ($Al(OH_3)$) at 25 °C, 1 bar; however, differences in pH dependence between corundum and gibbsite are negligible at these conditions. At 25 °C, 1 bar, metastable corundum solubility in H_2O displays a deep minimum of 1×10^{-7} molal at pH = 6.2 (Fig. 15A). Shifts in pH to more acidic or more alkaline values yield dramatic enhancement in dissolved Al concentration. The depth of the solubility minimum is partly a consequence of the fact that neutral $HAlO_{2(aq)}$ is only marginally stable at these conditions, and it accounts for the limited solubility of Al in near-neutral H_2O. Initially neutral H_2O acquires a very weakly acidic pH of 6.8 by equilibrating with corundum, and the dominant species is AlO_2^- (Fig. 15A).

As with calcite, the pH dependence of corundum solubility at 700 °C, 10 kbar, is similar in form to that at low *P* and *T* (Fig. 15B), but in detail there are important differences. The minimum in the solubility curve is substantially broader and shallower due to the significantly greater relative stability of neutral $HAlO_{2(aq)}$. The solubility of corundum is therefore predicted to be much higher at elevated *P* and *T*, consistent with experimental studies (Becker et al. 1983; Tropper and Manning 2007a). Neutral $HAlO_{2(aq)}$ is predicted to become predominant over AlO_2^- in initially pure H_2O equilibrated with corundum. Though the solution still shifts to slightly acid pH, the magnitude of this shift is smaller.

These conclusions have important implications for Al mobility as a consequence of H^+ metasomatism. At near-surface conditions, H^+ metasomatism leads to substantial Al solubility and mobility and is widely recognized where acidity is produced for example by oxidation and/or cooling of dissolved volcanic gases in hydrothermal systems. However, Figure 15B illustrates that acids do not have the same effect at high *P* and *T*, and the significant weakening of otherwise strong acids such as HCl (Fig. 12) at high-grade conditions makes it even more difficult to mobilize Al by this mechanism. Though H^+ metasomatism has been proposed in medium- to high-grade metamorphic contexts (Vernon 1979; Zaraisky 1994; Nabelek 1997; McLelland et al. 2002), the constraints imposed by Figure 15B make this scenario unlikely except in very unusual cases.

Buffering of pH by rock-forming minerals

The elevated log*K* for H_2O dissociation and the relative weakness of acids and bases at high *P* and *T* also mean that the nature of pH buffering by rock-forming mineral assemblages changes significantly with depth of metasomatic environment. For example, at ambient conditions, the consumption of H^+ during transformation of olivine to hydrous serpentine

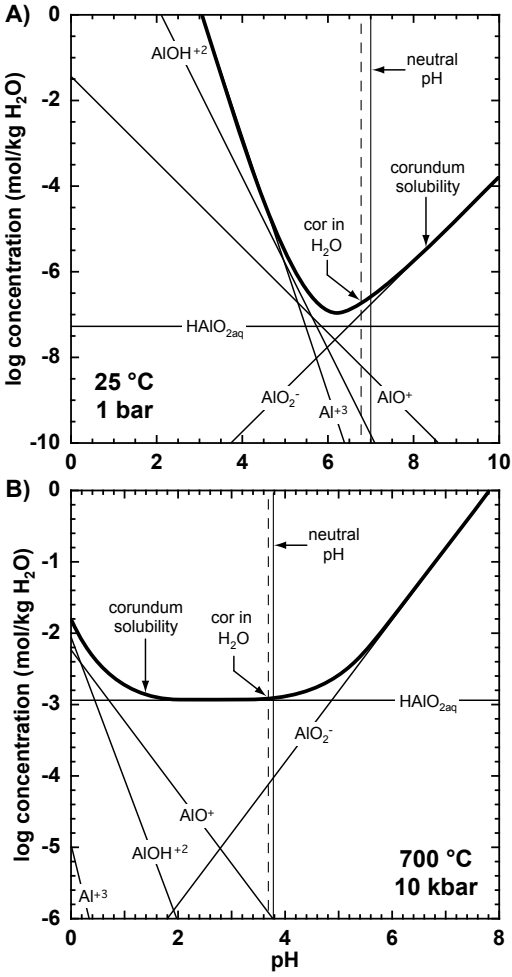

Figure 15. Solubility of corundum as a function of pH at 25 °C, 1 bar (A), and 700 °C, 10 kbar (B). Corundum solubility (bold line) is the sum of the concentrations of the Al species (thin lines). Vertical dashed lines show pH in pure H_2O equilibrated with corundum; vertical solid lines are neutral pH; intersection with the bold curve defines the solubility of calcite in H_2O; intersections with bold curves define the solubility of corundum in H_2O. Vertical solid line shows neutral pH. Figures calculated assuming unit activity coefficients. Mineral pH buffers calculated with density model with data from Marshall and Franck (1981), and SUPCRT92 using the slop98 data set. Abbreviation: cor, corundum.

minerals generates strongly alkaline waters. Springs issuing from actively serpentinizing ultramafic rocks may have pH in excess of 10 (e.g., Barnes and O'Neil 1969; Barnes et al. 1978). Does this also occur at high *P* and *T*? The relevant equilibria change with *P* and *T* due to variations in mineral stability; however, we can use the pH-buffering equilibrium between forsterite and talc

$$\underset{forsterite}{4Mg_2SiO_4} + 10H^+ = \underset{talc}{Mg_3Si_4O_{10}(OH)_2} + 5Mg^{+2} + 4H_2O \qquad (30)$$

as a model. Though this equilibrium is metastable with respect to others involving serpentine minerals at low *P* and *T*, it usefully illustrates how the consequences of H^+ consumption change with burial depth. At ambient conditions, pH buffered (metastably) by Equation (30) is 10.79, which differs from neutral pH (ΔpH) by 3.79 pH units. In geothermal systems of modest temperature (100 °C, P_{sat}), pH = 8.63 and ΔpH = 2.51. The disparity between the buffer equilibrium and neutrality is smaller, but buffered pH is still quite alkaline, consistent with observations of alkaline, ultramafic-hosted submarine warm springs (e.g., Kelley et al. 2001).

This trend continues as P and T increase: at 300 °C and 2 kbar, pH = 5.89 and ΔpH = 0.87; at 700 °C and 10 kbar, pH = 3.97 and ΔpH = 0.18. These calculations show that pH buffered by Equation (30) declines significantly with rising P and T. The buffered pH remains alkaline, as required by H^+ consumption (Eqn. 30); however, the most striking result is that the difference between buffered pH and neutrality declines to the point of insignificance at 700 °C and 10 kbar.

Similar results are obtained with other silicate pH buffers. At ambient conditions, the (metastable) assemblage K-feldspar + muscovite + quartz buffers pH at 9.40, whereas at 700 °C, pH is 4.09. As with forsterite + talc, ΔpH declines but remains alkaline—from 2.40 to 1.88. Note that, at 700 °C and 10 kbar, the pH buffered by the K-feldspar + muscovite + quartz is significantly more alkaline than that imposed by forsterite + talc. The results of these calculations indicate that as P and T increase to lower crustal and upper mantle conditions, less extreme pH shifts away from acid-base neutrality should be expected in fluids internally buffered by silicate rock mineral assemblages.

The effects of pH buffering by silicate mineral assemblages are important for deep fluids. Consider calcite, which is sparingly soluble in pure H_2O at 700 °C, 10 kbar. Figure 14B illustrates that aqueous pore fluids in which pH is controlled by equilibrium with a rock matrix dominated by silicate minerals such as K-feldspar + muscovite + quartz or forsterite + talc, will in effect act as moderate to strong acids and raise calcite solubility. For example, at forsterite-talc-buffered pH of 4.09, calcite solubility is 0.88 molal, or ~80 times higher than in H_2O equilibrated with calcite alone (Fig. 14B). Clearly, consideration of pH effects is essential in evaluating carbon transport in deep metasomatic environments.

Salinity and saline brines

Chlorine is likely an important ligand in high P-T fluids, and variation in its concentration will strongly influence dissolved element solubility and speciation. As discussed above, it is unlikely that externally derived solutions in these environments are strongly acidic. It is therefore more appropriate to examine the consequences of changing chlorinity by modeling Cl addition as a dissolved alkali-chloride, such as NaCl. Manning (1998) examined the role of varying dissolved NaCl concentration on solubilities of the model mineral assemblage glaucophane + garnet + omphacite + quartz near the blueschist-eclogite transition at 550 °C, 17.5 kbar (Fig. 16). Dissolved NaCl was varied from 0.001 to 1.0 molal, or 0.006 to 6 wt%. Figure 16 shows that Cl^- is the dominant form of chlorine in solution. Solute concentrations are generally low, even at the highest $[NaCl]_{total}$. Changes in speciation reflect the combination of the relative stabilities of association/dissociation equilibria and the large equilibrium constant for H_2O dissociation ($\log K = -6.91$).

As summarized by Newton and Manning (2010), highly concentrated brines may play an important role in high-grade metamorphism, especially at granulite-facies conditions in the lower crust. These brines may attain salt mole fractions of 0.3 or greater, and it is highly likely that the supporting cations include not just Na^+, but in addition K^+, Ca^{+2}, Mg^{+2}, and other major rock-forming metals. While a comprehensive treatment of these solutions is beyond the scope of this review, it is important to note that the standard state adopted here is inappropriate at such high concentrations. Newton and Manning (2010) showed that the brines can successfully be modeled as ideal solutions of fully dissociated salts diluted by H_2O. With the exception of quartz, solubilities of rock-forming minerals in such solutions are dramatically higher than in dilute aqueous solutions like those modeled in Figure 16 (Newton and Manning 2000, 2002, 2005, 2006, 2007, 2008a; Tropper and Manning 2007a,b; Antignano and Manning 2008a; Wykes et al. 2008; Tropper et al. 2011). Such solutions can be expected to be powerful metasomatic agents wherever they occur.

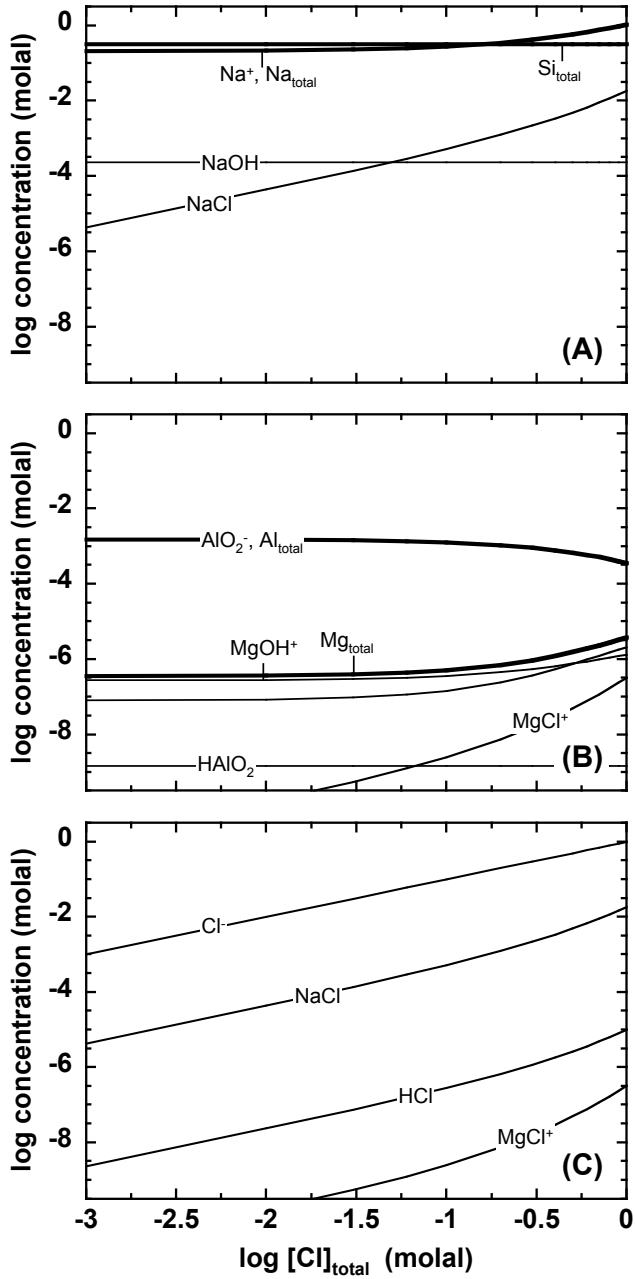

Figure 16. Variation in species concentrations with total Cl in aqueous fluid equilibrated with model glaucophane ecolgite at 550 °C, 17.5 kbar (after Manning 1998). Bold lines denote total element concentrations; thin lines, concentrations of individual species. The pH decreases from 6 to 5.3 as $\log Cl_{total}$ increases from −3 to 0; neutral pH is 3.5.

"Excess" solubility and identification of additional solutes

The methods described above also provide a framework for identifying new solute species and quantifying their concentrations. This is exemplified by experimental studies of the solubility of aqueous silica in equilibrium with various mineral assemblages. It was long assumed that in crustal metamorphic settings, all dissolved silica exists as monomeric silicic acid (H_4SiO_4, for which we will adopt here the anhydrous notation $SiO_{2(m)}$) (e.g., Walther and Helgeson 1977). This can be tested by comparing measured silica solubility associated with different assemblages which fix, or "buffer," the activity of SiO_2 at constant P and T. Examples are:

$$\underset{corundum}{Al_2O_3} + SiO_{2(m)} = \underset{kyanite}{Al_2SiO_5} \tag{31}$$

$$\underset{forsterite}{Mg_2SiO_4} + SiO_{2(m)} = \underset{enstatite}{2MgSiO_3} \tag{32}$$

If only monomeric SiO_2 is present, then assuming unit activity coefficient for neutral $SiO_{2(m)}$ (i.e., $\gamma_{SiO_{2(m)}} = a_{SiO_{2(m)}}$; see above) and stoichiometric minerals permits determination of the solubility of either assemblage constrains $\Delta G^\circ_{SiO_{2(m)}}$ at that P and T from:

$$\Delta G^\circ_{SiO_{2(m)}} = RT \ln m^{buffer}_{SiO_{2(m)}} + \Delta G^\circ_{kyanite} - \Delta G^\circ_{corundum} \tag{33}$$

Experimental measurements of SiO_2 concentrations associated with these assemblages (Zhang and Frantz 2000; Newton and Manning 2002, 2003) allow prediction of the solubility of other silica buffers, such as quartz:

$$\underset{quartz}{SiO_2} = SiO_{2(m)} \tag{34}$$

$$\ln m^{quartz}_{SiO_{2(m)}} = -\frac{\Delta G^\circ_{SiO_{2(m)}} - \Delta G^\circ_{quartz}}{RT} \tag{35}$$

which have been measured independently (e.g., Anderson and Burnham 1965; Manning 1994). Newton and Manning (2002, 2003) showed that using Equations (33) and (35) underpredicts quartz solubility at ≥5 kbar and ≥600 °C, and that the extent of underprediction grows with rising P and T. These observations require the presence of additional dissolved silica species whose concentrations increase with P and T. This is consistent with spectroscopic observation of polymerization of aqueous silica to form dimers ($Si_2O_{4(d)}$, Zotov and Keppler 2000 2002) at high P, T, and Si concentration. That is, the reaction

$$2SiO_{2(m)} = Si_2O_{4(d)} \tag{36}$$

is driven to the right at high P and T, and

$$[Si]_{total} = [SiO_{2(aq)}] = [SiO_{2(m)}] + 2[Si_2O_{4(d)}] \tag{37}$$

Figure 17 illustrates the consequences of recognizing the presence of SiO_2 dimers in addition to monomers. If all dissolved silica were assumed to be monomers and quartz solubility measurements alone had been used to derive $\Delta G^\circ_{SiO_{2(m)}}$, then the phase relations would predict more restricted stability fields than when polymerization is taken into account. Newton and Manning (2008b) and Hunt and Manning (2012) extended this approach to higher T and showed that further polymerization to trimers and other structures must occur as the hydrous melting curve is approached and crossed. As pointed out by Manning (2004), polymerization in the aqueous phase is the chemical behavior that makes possible fully miscible mixing of hydrous silicate melt and solute-rich aqueous fluid. Simple mixing models of the system SiO_2-H_2O that account for homogeneous polymerization reactions successfully reproduce melting relations and solubilities (Hunt and Manning 2012).

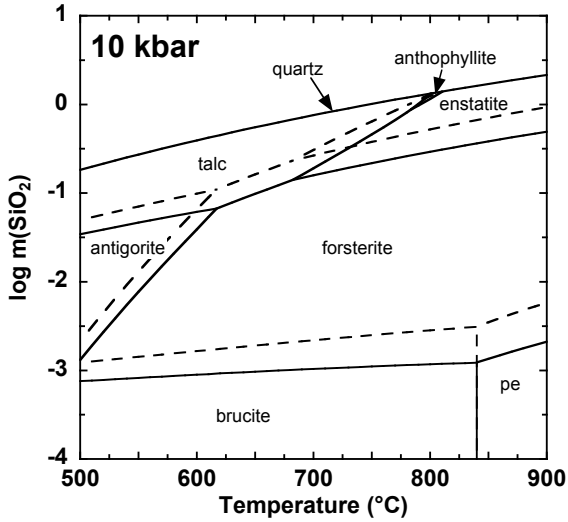

Figure 17. Equilibrium temperature-activity diagram depicting equilibrium phase relations in the system MgO-SiO_2-H_2O at 10 kbar (after Newton and Manning 2002). Dashed lines show phase relations assuming the presence of SiO_2 monomers only, derived from the solubility of quartz in H_2O (Manning 1994). Solid lines show phase relations accounting for the presence of silica monomers and dimers (Newton and Manning 2002). Abbreviation: pe, periclase.

Identification of excess solubility relative to that predicted via the density-model has been extended to other compositional systems and leads to the conclusion that aqueous polymerization of dissolved rock-forming oxide components is an unanticipated but pervasive feature of high-*PT* fluids. Manning (2007) identified Si and Al solubilities in corundum + kyanite equilibrated H_2O that were greater than predicted assuming only monomeric species of Si and Al (Fig. 18A). The excess solubility was used to predict the Gibbs free energy of an assumed Al-Si dimer, $HAlSiO_{4(aq)}$, and evaluate changes in species abundances as a function of addition of dissolved silica (Fig. 18B). Increasing $[Si]_{total}$ produces rising $[Al]_{total}$ due to increasing concentration of $HAlSiO_{4(aq)}$. This leads to the surprising prediction that the maximum dissolved Al concentration should be observed at quartz saturation rather than at corundum saturation, a result entirely a consequence of aluminosilicate cluster formation.

Manning et al. (2010) determined the solubility of the assemblage albite + paragonite + quartz at 350-620 °C, 10 kbar. Using simple dissolved solutes in this system, they showed that measured solubilities agreed with those predicted using the density-modeling approach at 350 to ~500 °C, indicating that calculations based on simple ions, monomers, and ion pairs of species in this system are adequate to explain the observations. However, measured solubilities are greater than predicted from 500 to 620 °C (Fig. 19). Moreover, the discrepancy grows with increasing *T*, and yields a predicted maximum at the melting point of 635 °C. The agreement at lower *T*, coupled with independent observations that density-based extrapolations are robust in simple solute systems even at higher *T* (see above), indicate that the discrepancy is caused by increasing concentrations of species not taken into account in the calculations; i.e., polymeric clusters. The results of Manning et al. (2010) make it clear that such species are in fact the most abundant solutes in the solutions. At the melting point, 81% of the dissolved solutes are in polymerized clusters. Polymerized silica is the most abundant dissolved constituent (6 wt%). Of this polymerized silica, 1.5 wt% is Si_2O_4 dimers and the rest is Si-Al, Si-Na, and Si-Al-Na clusters. Aluminum and sodium are present in roughly equal concentrations on a molar basis (Na/Al = 1.1). Similar conclusions have been reached for this system at higher *P* (Wohlers et al. 2011) and in the system K_2O-Al_2O_3-SiO_2-H_2O (Wohlers and Manning 2013).

Utilization of the density model for simple aqueous solutes for comparison with experimental results has thus led to critical insights into the important differences between

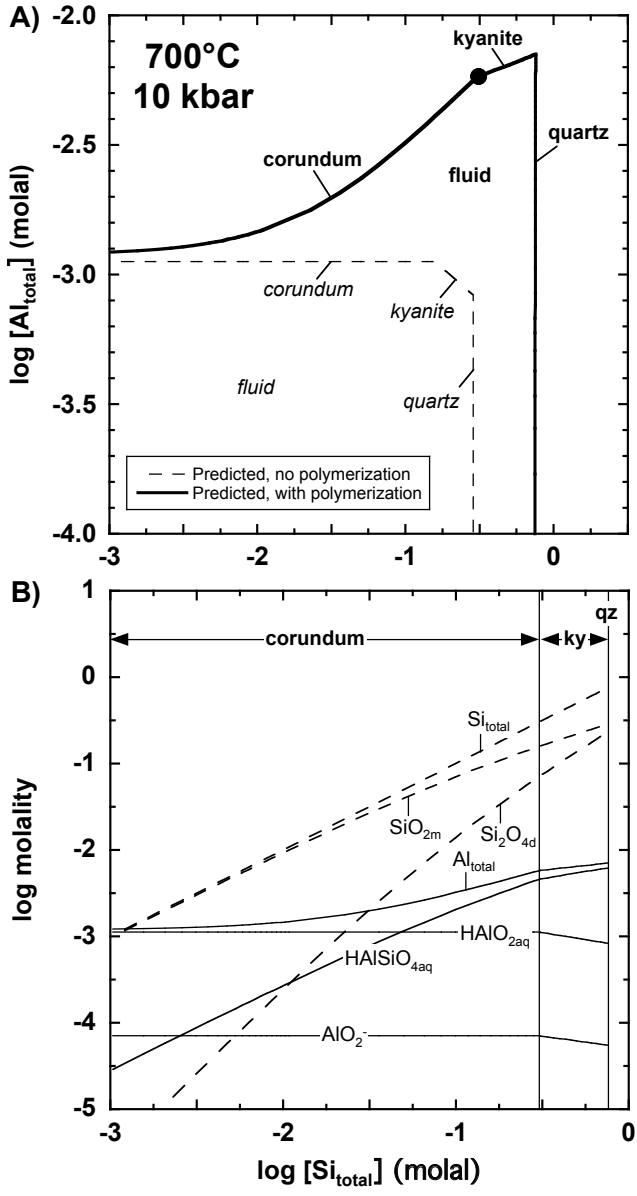

Figure 18. (A) Comparison of variations in predicted concentration of $[Al]_{total}$ and $[Si]_{total}$ with (solid lines) and without (dashed lines) polymerization at corundum, kyanite and quartz saturation, 700 °C, and 10 kbar (after Manning 2007). The filled circle denotes measure fluid composition from Manning (2007). The difference between the dashed and solid lines illustrates that Al_2O_3-SiO_2 and SiO_2 polymerization leads to significantly higher Al concentration, and the previously unexpected conclusion that maximum dissolved Al occurs at kyanite + quartz equilibrium rather than in equilibrium with corundum. (B) Equilibrium abundances of aqueous species coexisting with corundum, kyanite, and quartz, as a function of total Si molality at 700 °C, 10 kbar. Dashed lines, major Si species; solid lines, major Al species (after Manning 2007). Abbreviation: ky, kyanite.

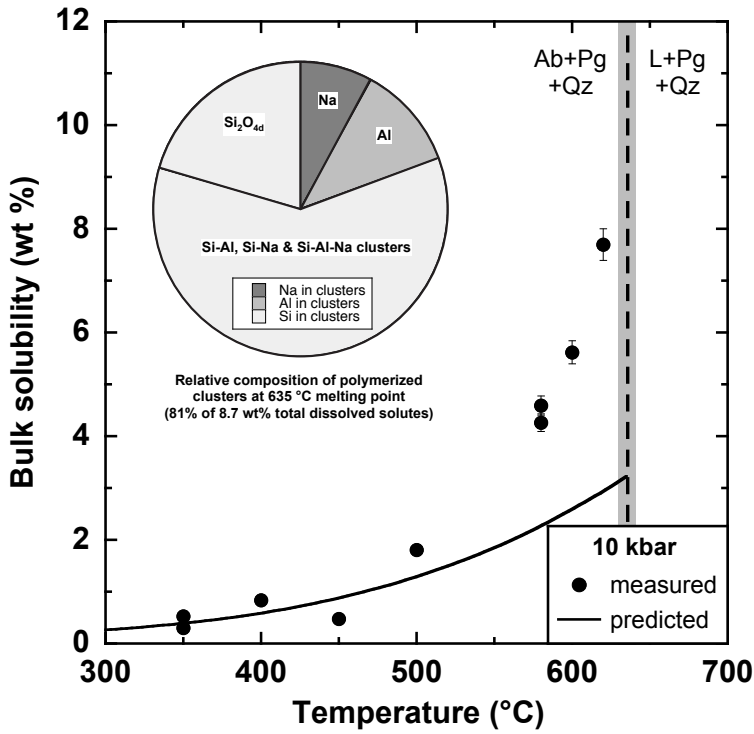

Figure 19. Comparison of experimentally determined and predicted solubilities of ablite + paragonite + quartz at 10 kbar (after Manning et al. 2010). Filled circles show experimental measurements; black line, predicted solubility using density-based modeling. Species used in the calculations were H^+, OH^-, Na^+, $NaOH_{(aq)}$, $HAlO_{2(aq)}$, AlO_2^-, $NaAlO_{2(aq)}$, $SiO_{2(m)}$, $Si_2O_{4(d)}$, and $NaHSiO_{3(aq)}$ ($HSiO_3^-$ was considered, but is omitted here). The divergence between predicted and measured bulk solubility indicates increasing concentrations of polymerized species. Inset shows the predicted relative composition of the 8.7 wt% of polymerized species at the solidus (635 °C), estimated from the difference between calculated solubility and extrapolation of the experimental results to the melting point.

shallow-crustal hydrothermal fluids and those in deep-crustal and upper mantle settings. The experimental observation that mineral solubilities are generally quite high at elevated *P* and *T* can be seen to arise in part from the tendency of rock forming oxides to form SiO_2-dominated polymeric clusters. Silica tends to be the most abundant dissolved solute in high a_{H_2O} fluids equilibrated with silicate rocks, so polymerized complexes with SiO_2 can be anticipated to be the predominant dissolved form of many elements. This is especially true for aluminum, for which low solubility in H_2O has long conflicted with ample geologic evidence for Al mobility as evidenced by aluminosilicates in high-*PT* veins and segregations (Manning 2007). The elevated Al solubility arising from the formation of polymerized Al-Si-hydroxide clusters offers a simple mechanism for dissolving and transporting significant Al. Similar conclusions have been drawn for elements such as Ti and Zr, whose oxides display low solubility in pure H_2O despite geologic evidence for fluid mobility in certain high *P* and *T* settings (Antignano and Manning 2008b; Manning et al. 2008; Ayers et al. 2012; Wilke et al. 2012; Louvel et al. 2013).

Concluding remarks

Thermodynamic modeling of interactions between aqueous fluids and rocks at high *P* and *T* require as input standard-state properties of solute species and a model for quantifying

departures from ideality. Work at middle crustal to upper mantle conditions has been hindered by uncertainties in solute properties and activity models at > 5 kbar. I have shown here that extrapolations based on the density of H_2O afford reasonable estimates of equilibrium constants and Gibbs free energies of equilibria and solutes. Moreover, calculations of the effects of non-ideality appear to be relatively insensitive to activity models and input parameters, at least to moderate total dissolved solids. Agreement between extrapolated data and experiment provides confidence for carrying out thermodynamic modeling of fluid-rock interaction at high *P* and *T*, which leads to the conclusion that fluids and their interaction with minerals differ in fundamental ways in deep terrestrial environments as compared to shallow settings.

The approach outlined must be viewed as an initial attempt to make deep fluid-rock interaction accessible to the widely used tools of aqueous geochemistry. The density-based approach has the advantages that it extends the commonly utilized HKF EOS, that any simple linear extrapolation is reasonable within HKF EOS uncertainties, that there is a thermodynamic basis for the approach to linearity, and that the range of extrapolation is relatively small. In addition, the approach allows simple combination of HKF data set with important homogeneous equilibria that are not included. On the other hand, the methods used are empirical, and the extrapolations will compound any errors in accuracy inherent to equations of state or experimental data. Mixing data sources can introduce serious accuracy and internal consistency problems. Nevertheless, the advantages strongly outweigh the shortcomings, as the approach makes possible quantitative aqueous geochemical modeling in a wide range of high-pressure geologic systems.

ACKNOWLEDGMENTS

This work was prepared while the author was in residence at the Lamont Doherty Earth Observatory of Columbia University. I thank P. Kelemen and T. Plank for their hospitality and probing discussions. The research was supported by grants from the National Science Foundation (EAR-1049901) and the Deep Carbon Observatory.

REFERENCES

Anderson GM, Burnham CW (1965) The solubility of quartz in supercritical water. Am J Sci 263:494-511

Anderson GM, Castet S, Schott J, Mesmer RE (1991) The density model for estimation of thermodynamic parameters of reactions at high temperatures and pressures. Geochim Cosmochim Acta 55:1769-1779

Antignano A, Manning CE (2008a) Fluorapatite solubility in H_2O and H_2O-NaCl at 700 to 900 °C and 0.7 to 2.0 GPa. Chem Geol 251:112-119

Antignano A, Manning CE (2008b) Rutile solubility in H_2O, H_2O-SiO_2, and H_2O-$NaAlSi_3O_8$ fluids at 0.7-2.0 GPa and 700-1000 °C: Implications for mobility of nominally insoluble elements. Chem Geol 255:283-293

Aranovich LY, Newton RC (1996) H_2O activity in concentrated NaCl solutions at high pressures and temperatures measured by the brucite-periclase equilibrium. Contrib Mineral Petrol 125:200-212

Aranovich LY, Newton RC (1997) H_2O activity in concentrated KCl and KCl-NaCl solutions at high temperatures and pressures measured by the brucite-periclase equilibrium. Contrib Mineral Petrol 127:261-271

Aranovich LY, Newton RC, Manning CE (2013) Brine-assisted anatexis: experimental melting in the system haplogranite-H_2O-NaCl-KCl at deep-crustal conditions. Earth Planet Sci Lett, doi: 10.1016/j.epsl.2013.05.027

Ayers J, Zhang L, Luo Y, Peters T (2012) Zircon solubility in alkaline aqueous fluids at upper crustal conditions. Geochim Cosmochim Acta 96:18-28

Ayers JC, Brenan JB, Watson EB, Wark DA, Minarik WG (1992) A new capsule technique for hydrothermal experiments using the piston-cylinder apparatus. Am Mineral 77:1080-1086

Barnes I, O'Neil JR (1969) The relationship between fluids in some fresh Alpine-type ultramafics and possible modern serpentinization, western United States. Geol Soc Am Bull 80:1947-1960

Barnes I, O'Neil JR, Trescases JJ (1978) Present day serpentinization in New Caledonia, Oman and Yugoslavia. Geochim Cosmochim Acta 42:144-145

Bassett WA, Wu T-C, Chou I-M, Haselton HT Jr., Frantz J, Mysen BO, Huang W-L, Sharma SK, Schiferl D (1996) The hydrothermal diamond anvil cell (HDAC) and its applications. *In:* Mineral Spectroscopy: A Tribute to Roger G. Burns. Dyar MD, McCammon C, Schaefer MW (eds) The Geochemical Society, Special Publication No. 5, p 261-272

Becker KH, Cemic L, Langer KEOE (1983) Solubility of corundum in supercritical water. Geochim Cosmochim Acta 47:1573-1578

Bowers TS, Jackson KJ, Helgeson HC (1984) Equilibrium activity diagrams: for coexisting minerals and aqueous solutions at pressures and temperatures to 5 kb and 600 °C. Springer, Berlin

Caciagli NC, Manning CE (2003) The solubility of calcite in water at 6-16 kbar and 500-800 °C. Contrib Mineral Petrol 146:275-285

Davies CW (1938) The extent of dissociation of salts in water. Part VIII. An equation for the mean ionic activity coefficient of an electrolyte in water, and a revision of the dissociation constants of some sulphates. J Chem Soc 1938:2093-2098

Davies CW (1962) Ion Association. Butterworths, Washington, D.C.

Dolejš D (2013) Thermodynamics of aqueous species at high temperatures and pressures: equations of state and transport theory. Rev Mineral Geochem 76:35-79

Dolejš D, Manning CE (2010) Thermodynamic model for mineral solubility in aqueous fluids: theory, calibration and application to model fluid-flow systems. Geofluids 10:20-40

Eugster HP, Baumgartner L (1987) Mineral solubilities and speciation in supercritical metamorphic fluids. Rev Mineral 17:367-403

Fernández DP, Goodwin ARH, Lemmon EW, Levelt Sengers JMH, Williams RCA (1997) A formulation for the static permittivity of water and steam at temperatures from 238 K to 873 K at pressures up to 1200 MPa, including derivatives and Debye-Huckel coefficients. J Phys Chem Ref Data 26:1125-1166

Fournier RO, Potter RW II (1982) An equation correlating the solubility of quartz in water from 25° to 900 °C at pressures up to 10,000 bars. Geochim Cosmochim Acta 46:1969-1973

Franck EU (1956) Hochverdichteter Wasserdampf III. Ionen-dissoziation von HCl, KOH und Wasser. Z Phys Chem 6:192-206

Franck EU, Rosenzweig S, Christoforakos M (1990) Calculation of the dielectric constant of water to 1000 °C and very high pressures. Bunsen-Ges Phys Chem 94:199-203

Frantz JD, Marshall WL (1982) Electrical conductances and ionization constants of calcium chloride and magnesium chloride in aqueous solutions at temperatures to 600 °C and pressures to 4000 bars. Am J Sci 282:1666-1693

Frantz JD, Marshall WL (1984) Electrical conductances and ionization constants of salts, acids, and bases in supercritical aqueous fluids: 1. Hydrochloric-acid from 100° to 700 °C and at pressures to 4000 bars. Am J Sci 284:651-667

Haar L, Gallagher JS, Kell GS (1984) NBS/NRC Steam Tables. Hemisphere, New York

Heger K, Uematsu M, Franck EU (1980) The static dielectric constant of water at high pressures and temperatures to 500 MPa and 550°C. Ber Bunsen Ges Phys Chem 84:758-762

Helgeson HC (1969) Thermodynamics of hydrothermal systems at elevated temperatures and pressures. Am J Sci 267:729-804

Helgeson HC, Kirkham DH (1974) Theoretical prediction of the thermodynamic behavior of aqueous electrolytes at high pressures and temperatures: II. Debye-Hückel parameters for activity coefficients and relative partial molal properties. Am J Sci 274:1199-1261

Helgeson HC, Kirkham DH (1976) Theoretical prediction of the thermodynamic behavior of aqueous electrolytes at high pressures and temperatures: III. Equation of state for aqueous species at infinite dilution. Am J Sci 276:97-240

Helgeson HC, Kirkham DH, Flowers GC (1981) Theoretical prediction of the thermodynamic behavior of aqueous electrolytes at high pressures and temperatures: IV. Calculation of activity coefficients, osmotic coefficients, and apparent molal and standard and relative partial molal properties to 600 °C and 5 kb. Am J Sci 281:1249-1516

Ho PC, Palmer DA (1997) Ion association of dilute aqueous potassium chloride and potassium hydroxide solutions to 600 °C and 300 MPa determined by electrical conductance measurements. Geochim Cosmochim Acta 61:3027-3040

Holland TJB, Powell R (1998) An internally consistent thermodynamic data set for phases of petrological interest. J Metamorph Geology 16:309-343, doi: 10.1111/j.1525-1314.1998.00140.x

Hunt JD, Manning CE (2012) A thermodynamic model for the system SiO_2-H_2O near the upper critical end point based on quartz solubility experiments at 500-1100 °C and 5-20 kbar. Geochim Cosmochim Acta 86:196-213

Johnson JW, Oelkers EH, Helgeson HC (1992) SUPCRT92: A software package for calculating the standard molal thermodynamic properties of minerals, gases, aqueous species, and reactions from 1 to 5000 bar and 0 to 1000 °C. Computers & Geosciences 18:899-947

Kelley DS, Karson JA, Blackman DK, Fruh-Green GL, Butterfield DA, Lilley MD, Olson EJ, Schrenk MO, Roe KK, Lebon GT, Rivizzigno P, Party ATS (2001) An off-axis hydrothermal vent field near the Mid-Atlantic Ridge at 30°N. Nature 412:145-149

Louvel M, Sanchez-Valle C, Malfait WJ, Testemale D, Hazemann JL (2013) Zr complexation in high pressure fluids and silicate melts and implications for the mobilization of HFSE in subduction zones. Geochim Cosmochim Acta 104:281-299

Manning CE (1994) The solubility of quartz in H_2O in the lower crust and upper mantle. Geochim Cosmochim Acta 58:4831-4839

Manning CE (1998) Fluid composition at the blueschist-eclogite transition in the model system Na_2O-MgO-Al_2O_3-SiO_2-H_2O-HCl. Schweiz Mineral Petrogr Mitt 78:225-242

Manning CE (2004) The chemistry of subduction-zone fluids. Earth Planet Sci Lett 223:1-16

Manning CE (2007) Solubility of corundum plus kyanite in H_2O at 700 °C and 10 kbar: evidence for Al-Si complexing at high pressure and temperature. Geofluids 7:258-269

Manning CE, Antignano A, Lin HA (2010) Premelting polymerization of crustal and mantle fluids, as indicated by the solubility of albite + paragonite + quartz in H_2O at 1 GPa and 350-620 °C. Earth Planet Sci Lett 292:325-336

Manning CE, Boettcher SL (1994) Rapid-quench hydrothermal experiments at mantle pressures and temperatures. Am Mineral 79:1153-1158

Manning CE, Shock EL, Sverjensky DA (2013) The chemistry of carbon in aqueous fluids at crustal and upper-mantle conditions: experimental and theoretical constraints. Rev Mineral Geochem 75:109-148

Manning CE, Wilke M, Schmidt C, Cauzid J (2008) Rutile solubility in albite-H_2O and $Na_2Si_3O_7$-H_2O at high temperatures and pressures by in-situ synchrotron radiation micro-XRF. Earth Planet Sci Lett 272:730-737

Marshall WL, Franck EU (1981) Ion product of water substance, 0-1000 °C, 1-10,000 bars: new international formulation and its background. J Phys Chem Ref Data 10:295-304

Marshall WL, Mesmer RE (1984) Pressure-density relationships and ionization equilibria in aqueous solutions. J Solution Chem 13:383-391

Marshall WL, Quist AS (1967) A representation of isothermal ion–ion-pair–solvent equilibria independent of changes in dielectric constant. Proc Natl Acad Sci USA 58:901-906

McLelland J, Morrison J, Selleck B, Cunningham B, C. O, Schmidt K (2002) Hydrothermal alteration of late- to post-tectonic Lyon Mountain Granite Gneiss, Adirondack Mountains, New York: origin of quartz-sillimanite segregations, quartz-albite lithologies and associated Kiruna-type low-Ti Fe-oxide deposits. J Metamorph Geol 20:175-190

Mesmer RE (1991) A new approach to measuring pH in brines and other concentrated electrolytes - comment. Geochim Cosmochim Acta 55:1175-1176

Mesmer RE, Marshall WL, Palmer DA, Simonson JM, Holmes HF (1988) Thermodynamics of aqueous association and ionization reactions at high temperatures and pressures. J Solution Chem 17:699-718

Nabelek PI (1997) Quartz-sillimanite leucosomes in high-grade schists, Black Hills, South Dakota: A perspective on the mobility of Al in high-grade metamorphic rocks. Geology 25:995-998

Newton RC, Aranovich LY, Hansen EC, Vandenheuvel BA (1998) Hypersaline fluids in Precambrian deep-crustal metamorphism. Precambrian Res 91:41-63

Newton RC, Manning CE (2000) Quartz solubility in H_2O-NaCl and H_2O-CO_2 solutions at deep crust-upper mantle pressures and temperatures: 2-15 kbar and 500-900°C. Geochim Cosmochim Acta 64:1993-3005

Newton RC, Manning CE (2002) Solubility of silica in equilibrium with enstatite, forsterite, and H_2O at deep crust/upper mantle pressures and temperatures and an activity-concentration model for polymerization of aqueous silica. Geochim Cosmochim Acta 66:4165-4176

Newton RC, Manning CE (2003) Activity coefficient and polymerization of aqueous silica at 800 °C, 12 kbar, from solubility measurements on SiO_2-buffering mineral assemblages. Contrib Mineral Petrol 146:135-143

Newton RC, Manning CE (2005) Solubility of anhydrite, $CaSO_4$, in NaCl-H_2O solutions at high pressures and temperatures: applications to fluid-rock interaction. J Petrol 46:701-716

Newton RC, Manning CE (2006) Solubilities of corundum, wollastonite and quartz in H_2O-NaCl solutions at 800 °C and 10 kbar: Interaction of simple minerals with brines at high pressure and temperature. Geochim Cosmochim Acta 70:5571-5582

Newton RC, Manning CE (2007) Solubility of grossular, $Ca_3Al_2Si_3O_{12}$, in H_2O-NaCl solutions at 800 °C and 10 kbar, and the stability of garnet in the system $CaSiO_3$-Al_2O_3-H_2O-NaCl. Geochim Cosmochim Acta 71:5191-5202

Newton RC, Manning CE (2008a) Solubility of corundum in the system Al_2O_3-SiO_2-H_2O-NaCl at 800 °C and 10 kbar. Chem Geol 249:250-261

Newton RC, Manning CE (2008b) Thermodynamics of SiO_2-H_2O fluid near the upper critical end point from quartz solubility measurements at 10 kbar. Earth Planet Sci Lett 274:241-249

Newton RC, Manning CE (2010) Role of saline fluids in deep-crustal and upper-mantle metasomatism: insights from experimental studies. Geofluids 10:58-72

Oelkers EH, Helgeson HC (1991) Calculation of activity coefficients and degrees of formation of neutral ion pairs in supercritical electrolyte solutions. Geochim Cosmochim Acta 55:1235-1251

Pan D, Spanu L, Harrison B, Sverjensky DA, Galli G (2013) The dielectric constant of water under extreme conditions and transport of carbonates in the deep Earth. Proc Natl Acad Sci USA 110:6646-6650

Pitzer KS (1977) A thermodynamic model for aqueous solutions of liquid-like density. Rev Mineral 17:97-142

Pitzer KS (1979) Theory: ion interaction approach. *In*: Activity Coefficients in Electrolyte Solutions. Pytkowitz RM (ed) CRC Press, Boca Raton, p 157-208

Pitzer KS (1983) Dielectric constant of water at very high temperature and pressure. Proc Natl Acad Sci USA 80:4575-4576

Plyasunov AV, Shock EL (2001) Correlation strategy for determining the parameters of the revised Helgeson-Kirkham-Flowers model for aqueous nonelectrolytes. Geochim Cosmochim Acta 65:3879-3900

Pokrovskii VA, Helgeson HC (1995) Thermodynamic properties of aqueous species and the solubilities of minerals at high pressures and temperatures: the system Al_2O_3-H_2O-NaCl. Am J Sci 295:1255-1342

Pokrovskii VA, Helgeson HC (1997) Thermodynamic properties of aqueous species and the solubilities of minerals at high pressures and temperatures: the system Al_2O_3-H_2O-KOH. Chem Geol 137:221-242

Quist AS (1970) The ionization constant of water to 800° and 4000 bars. J Phys Chem 74:3396-3402

Quist AS, Marshall WL (1968a) Electrical conductances of aqueous sodium chloride solutions from 0 to 800° and pressures to 4000 bars. J Phys Chem 68:684-703

Quist AS, Marshall WL (1968b) Ionization equilibria in ammonia-water solutions to 700 °C and to 4000 bars pressure. J Phys Chem 72:3122-3128

Saul A, Wagner W (1989) A fundamental equation for water covering the range from the melting line to 1273 K at pressures up to 25000 MPa. J Phys Chem Ref Data 18:1537-1564

Shock EL, Helgeson HC (1988) Calculation of the thermodynamic and transport properties of aqueous species at high pressures and temperatures: correlation algorithms for ionic species and equation of state predictions to 5 kb and 1000 °C. Geochim Cosmochim Acta 52:2009-2036

Shock EL, Helgeson HC (1990) Calculation of the thermodynamic and transport properties of aqueous species at high pressures and temperatures: Standard partial molal properties of organic species. Geochim Cosmochim Acta 54:915-945

Shock EL, Helgeson HC, Sverjensky DA (1989) Calculation of the thermodynamic and transport properties of aqueous species at high pressures and temperatures: standard partial molal properties of inorganic neutral species. Geochim Cosmochim Acta 53:2157-2183

Shock EL, Oelkers EH, Johnson JW, Sverjensky DA, Helgeson HC (1992) Calculation of the thermodynamic and transport properties of aqueous species at high pressures and temperatures: Effective electrostatic radii to 1000 °C and 5 kb. J Chem Soc Faraday Trans 88:803-826

Shock EL, Sassani DC, Willis M, Sverjensky DA (1997) Inorganic species in geologic fluids: correlations among standard molal thermodynamic properties of aqueous ions and hydroxide complexes. Geochim Cosmochim Acta 61:907-950

Sverjensky DA, Shock EL, Helgeson HC (1997) Prediction of the thermodynamic properties of aqueous metal complexes to 1000 °C and 5 kb. Geochim Cosmochim Acta 61:1359-1412

Sweeton FH, Mesmer RE, Baes CF (1974) Acidity measurements at elevated temperatures. VII. Dissociation of water. J Solution Chem 3:191-214

Syracuse EM, van Keken PE, Abers GA (2010) The global range of subduction zone thermal models. Phys Earth Planet Interior 183:73-90

Tanger JC, IV, Helgeson HC (1988) Calculation of the thermodynamic and transport properties of aqueous species at high pressures and temperatures: revised equations of state for the standard partial molal preperties of ions and electrolytes. Am J Sci 288:19-98

Touret JLR (1985) Fluid regime in southern Norway: the record of fluid inclusions. *In*: The Deep Proterozoic Crust in the North Atlantic Provinces. Tobi AC, Touret JLR (eds) Reidel, Dordecht, p 517-549

Tropper P, Manning CE (2007a) The solubility of corundum in H_2O at high pressure and temperature and its implications for Al mobility in the deep crust and upper mantle. Chem Geol 240:54-60

Tropper P, Manning CE (2007b) The solubility of fluorite in H_2O and H_2O-NaCl at high pressure and temperature. Chem Geol 242:299-306

Tropper P, Manning CE, Harlov DE (2011) Solubility of $CePO_4$ monazite and YPO_4 xenotime in H_2O and H_2O-NaCl at 800 °C and 1 GPa: Implications for REE and Y transport during high-grade metamorphism. Chem Geol 282:58-66

Vernon RH (1979) Formation of late sillimanite by hydrogen metasomatism (base-leaching) in some high-grade gneisses. Lithos 12:143-152

Wagner W, Pruß A (2002) The IAPWS formulation 1995 for the thermodynamic properties of ordinary water substance for general and scientific use. J Phys Chem Ref Data 31:387-535

Walther JV, Helgeson HC (1977) Calculation of the thermodynamic properties of aqueous silica and the solubility of quartz and its polymorphs at high pressures and temperatures. Am J Sci 277:1315-1351

Wilke M, Schmidt C, Dubrail J, Appel K, Borchert M, Kvashnina K, Manning CE (2012) Zircon solubility and zirconium complexation in H_2O-Na_2O-SiO_2-Al_2O_3 fluids at high pressure and temperature. Earth Planet Sci Lett 349:15-25

Wohlers A, Manning CE (2009) Solubility of corundum in aqueous KOH solutions at 700 °C and 1 GPa. Chem Geol 262:310-317

Wohlers A, Manning CE (2013) Solubility of K-feldspar, muscovite and corundum in H_2O, with and without quartz at 700 °C and 1 GPa: Implications for high-pressure fluid-mineral interaction in model pelitic and granitic systems. Geochimica et Cosmochimica Acta (submitted)

Wohlers A, Manning CE, Thompson AB (2011) Experimental investigation of the solubility of albite and jadeite in H_2O, with paragonite plus quartz at 500 and 600 °C, and 1-2.25 GPa. Geochim Cosmochim Acta 75:2924-2939

Wykes JL, Newton RC, Manning CE (2008) Solubility of andradite, $Ca_3Fe_2Si_3O_{12}$, in a 10 mol% NaCl solution at 800 °C and 10 kbar: Implications for the metasomatic origin of grandite garnet in calc-silicate granulites. Am Mineral 93:886-892

Zaraisky GP (1994) The influence of acidic fluoride and chloride solutions on the geochemical behaviour of Al, Si and W. *In*: Fluids in the Crust: Equilibrium and Transport Properties. Shmulovich KI, Yardley BWD, Gonchar CG (eds) Chapman and Hall, London, p 139-162

Zhang YG, Frantz JD (2000) Enstatite-forsterite-water equilibria at elevated temperatures and pressures. Am Mineral 85:918-925

Zotov N, Keppler H (2000) In-situ Raman spectra of dissolved silica species in aqueous fluids to 900 °C and 14 kbar. Am Mineral 85:600-604

Zotov N, Keppler H (2002) Silica speciation in aqueous fluids at high pressures and high temperatures. Chem Geol 184:71-82